Macromolecules

Article

pubs.acs.org/Macromolecules

Anisotropic Three-Particle Interactions between Spherical Polymer-Grafted Nanoparticles in a Polymer Matrix

Tsung-Yeh Tang and Gaurav Arya*

Department of NanoEngineering, University of California, San Diego, 9500 Gilman Drive, Mail Code 0448, La Jolla, California 92093, United States

Supporting Information

ABSTRACT: Spherical nanoparticles (NPs) uniformly grafted with polymer chains have recently been shown to assemble into anisotropic phases like strings and sheets. Here we investigated the underlying basis for anisotropic interactions between polymer-grafted NPs in a polymer matrix by computing via molecular dynamics simulations the potential of mean force (PMF), and its three-body contribution, for a test NP interacting with a NP-dimer along a set of reaction coordinates differing in their orientation with respect to the dimer axis. The polymer-mediated portions of the PMF and of the three-body contribution were both found to be highly repulsive and anisotropic with the degree of repulsion rising with increasing angular deviation from the dimer axis. The anisotropy was shown to arise from the expulsion of polymer grafts from in between the dimer NPs which leads to a gradient in the graft segmental density around the dimer from its contact point to its poles. This effect produces a concomitant gradient in steric repulsion between test and dimer NP grafts, a significant portion of which is however negated by an opposing gradient in depletion attraction between NPs due to the matrix. The anisotropy in the polymer-mediated PMF was observed to be particularly strong for NP−polymer systems with long grafts, high grafting densities, and short matrix chains. The overall PMFs allowed us to compute the free energies of formation of two- and three-particle clusters, yielding a phase diagram in graft length−grafting density parameter space analogous to that observed experimentally for the dispersed, stringlike, and sheetlike phases of NPs. The PMFs also revealed possible existence of a stable dimer phase that remains to be tested experimentally. Taken together, this study illustrates how the deformability of NP grafts can introduce novel anisotropic interactions between otherwise isotropic NPs with far-reaching consequences in NP assembly.

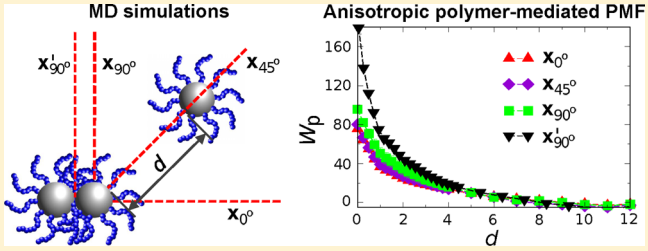

INTRODUCTION

An emerging concept in materials science is the engineering of anisotropic interactions between nanoparticle (NP) building blocks to drive their self-assembly into higher-order structures more complex than the random aggregates or simple close-packed lattices nominally obtained from spherical NPs.[1,2] Anisotropic interactions are most intuitively achieved by using particle shapes that go beyond simple spheres,[3] that is, by exploiting the inherent anisotropy in the excluded volume interactions between "shaped" NPs. Materials chemists are now able to synthesize a rich variety of particle shapes, ranging from simple rods and discs to more exotic ones like cones, tetrapods, and various kinds of polyhedra,[3−7] and assemble them into anisotropic structures with some degree of success.[8−10] Alternatively, the surface of NPs may be grafted or coated with chemical ligands in an anisotropic manner to produce gradients or discrete patches of ligands. Such "patchy" NPs may be designed to exhibit anisotropic steric repulsion through polymer grafting,[11,12] anisotropic attraction through grafting of sticky molecules such as single-stranded DNA,[13] or anisotropic response to external fields like magnetic fields.[14]

Recent studies however suggest that even NPs exhibiting isotropic two-body interaction potentials may assemble into anisotropic structures.[15−17] The most striking evidence comes from experiments on the assembly of spherical silica NPs uniformly grafted with polystyrene chains within a polystyrene matrix.[17] It was found that, in addition to exhibiting dispersed and densely packed aggregate phases expected of isotropic particles, these NPs also assembled into anisotropic structures like 1D strings and 2D sheets, depending on the length and surface density of their polymer grafts. Similar anisotropic phases have been observed in other grafted-NP systems as well[18−21] and also realized in molecular dynamics and Monte Carlo simulations of simplified models of polymer-grafted NPs.[17,18,22] To explain the observed "phase diagram", it was proposed that the free energy of each phase is determined by a competition between favorable enthalpic energy gained by forming contacts between NPs and the entropic cost associated with compressing the polymer grafts to form such contacts.[22] In general, the higher the dimensionality of a phase, the larger the number of favorable contacts its NPs exhibit and the stronger the confinement that their grafted chains experience. By using

Received: September 1, 2016
Revised: December 10, 2016

DOI: 10.1021/acs.macromol.6b01936
Macromolecules XXXX, XXX, XXX−XXX

simple scaling relationships for the two effects, structures with the lowest free energy were determined at various points across the parameter space, yielding a phase diagram that qualitatively agreed with that observed experimentally.

Key to the unusual stability of anisotropic structures in polymer-grafted NPs is the anisotropic distribution of polymer grafts that is supposed to develop when NPs come into close contact.[17,18,22] Specifically, approaching NPs push aside the intervening polymer grafts, causing an increase in polymer density near the contact region of the NPs. This effect is believed to introduce an anisotropic steric repulsion felt by a third approaching NP, wherein the dimer becomes more susceptible to binding by the third NP at its two poles on the longitudinal axis as compared to the contact region, thus providing a natural driving force for the assembly of NPs into 1D strings. One would also presume that this steric repulsion increases as one moves away from the NP poles and toward the contact region, and hence, binding of NPs at other locations along this path may be favored if the steric repulsion at those locations can be compensated by additional favorable contacts between the ensuing higher-order structures. Indeed, in the absence of any such emergent three-body anisotropic interactions arising from the polymer, the NPs would either assemble into 3D hexagonally close-packed ("isotropic") structures that maximize the number of attractive contacts between NPs or else remain dispersed if the attraction was sufficiently weak.

Here we investigate such polymer rearrangement-based origin of anisotropic interactions between polymer-grafted NPs, a key *hypothesis* that has not been tested thus far. Our approach involves using molecular dynamics (MD) simulations of coarse-grained models of the NP−polymer system to directly compute the potential of mean force of interaction between an isolated NP and a NP-dimer as a function of their relative separation and orientation and to relate any observed anisotropy in the computed interaction to that in the polymer conformations and density. Our results provide the first direct confirmation of the above hypothesis and reveal new insights into how the grafted and matrix polymer conspire to produce anisotropic interactions between NPs. We further demonstrate how variations in anisotropic interactions with respect to parameters like NP-graft length, grafting density, and interparticle-attraction strength lead to intriguing "phase behavior" among various NP cluster configurations, including a novel globally stable dimer phase whose existence remains to be tested experimentally.

COMPUTATIONAL METHODS

System Design and Configuration. Our aim is to investigate the anisotropy in the free energy of interactions—the potential of mean force (PMF)—between an isolated polymer-grafted NP termed "test" NP and a preassembled dimer of polymer-grafted NPs in a polymer matrix and to examine how such interactions lead to anisotropic structures. Because of the symmetry of the dimer, the PMF can be described in terms of two coordinates: the center-to-center distance r between the test NP and one of the dimer NPs (see Figure 1a) and the angle θ subtended by the line connecting the centers of these two NPs with the longitudinal axis of the dimer for characterizing the anisotropy in the system. Note that the angle varies in the range $\theta = [0, \pi - \cos^{-1}(d_0/2r)]$, where d_0 is the fixed center-to-center distance between the two dimer NPs (Figure 1a).

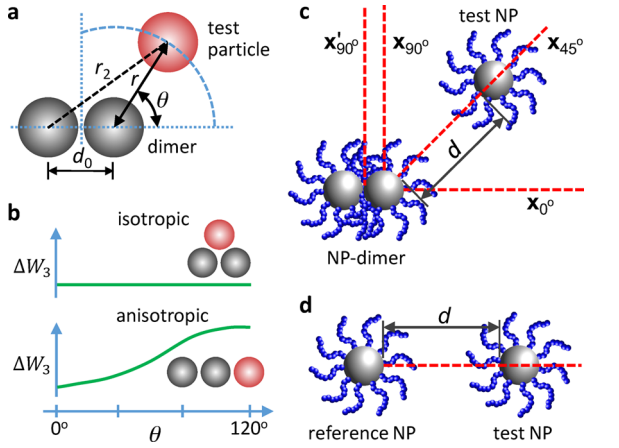

Figure 1. (a) Coordinate system used for describing anisotropic interactions in a three-particle system. The test and dimer particles are identical but shown in different color for clarity. (b) Schematic illustrating how a strong angular dependence (anisotropy) in the three-body PMF ΔW_3 can cause particles to assemble into anisotropic structures. (c) Schematic showing the four reaction coordinates chosen for examining the anisotropy in three-particle interactions between polymer-grafted NPs. The NP cores are shown as gray circles and the polymer grafts as blue chains. The polymer matrix is not shown for clarity. (d) Schematic showing the reaction coordinate used for computing the isotropic two-particle interactions. All interactions were computed as a function of the surface-to-surface distance d between the test NP and the reference NP cores (or those of the nearest dimer NP).

To define "anisotropic structures" and "anisotropic interactions" in the context of such a three-particle system, we consider a simpler example where we replace the polymer matrix with vacuum and replace the polymer-grafted NPs with single particles that interact with each other via a pairwise-additive isotropic potential $U(r)$ exhibiting a single minimum at $r = r_{min}$. Since the interaction depends on a single degree of freedom (r), the two-body PMF $W_2(r)$ for this interaction is simply equal to $U(r)$. The *overall* three-particle PMF $W(r,\theta)$ for the interaction between the test particle and the dimer is equal to the sum of the two-body PMFs of the test particle with each of the two dimer particles: $W(r,\theta) = W_2(r) + W_2(r_2)$, where r and $r_2 \equiv r_2(r,\theta)$ are the separation distances between the test particle and the two dimer particles. Thus, the overall PMF depends on the orientation angle θ (due to the interaction $W_2(r_2)$ arising from the one of the dimer particles) and is therefore anisotropic. The most stable state of such a system is obviously one in which the test particle sits symmetrically atop the dimer at a separation distance of $r = r_2 = r_{min}$ and $\theta = \pi - \cos^{-1}(d_0/2r_{min})$ coinciding with the minima of both the two-body PMFs. We define this compact, assembled state of particles as the "isotropic structure" for the three-particle system, and all other configurations such as the linear configuration of the three particles (where $\theta = 0$) are termed as "anisotropic structures".

The above example clearly demonstrates that (1) the anisotropy in the overall PMF $W(r,\theta)$ is *not* the most appropriate indicator of the formation of anisotropic structures and (2) overall PMFs that can be written as the pairwise sum of isotropic two-body PMFs exhibiting a single energy minimum will always form isotropic structures. Anisotropic structures in such systems must therefore arise from multibody contributions, or three-body contributions in the context of three-

DOI: 10.1021/acs.macromol.6b01936
Macromolecules XXXX, XXX, XXX−XXX

particle systems. The overall three-particle PMF is then given by $W(r,\theta) = W_2(r) + W_2(r_2) + \Delta W_3(r,\theta)$, where ΔW_3 represents the three-body contribution that likely depends on r and θ. Thus, if ΔW_3 exhibits a strong angular dependence (anisotropy), it allows for the possibility of anisotropic structures becoming more stable than isotropic structures, e.g., when ΔW_3 is much larger for isotropic than anisotropic configurations (Figure 1b). Hence, we define "isotropic interactions" by interactions that either lead to negligible $\Delta W_3(r,\theta)$ or angle-independent $\Delta W_3(r,\theta) \approx \Delta W_3(r)$, whereas "anisotorpic interactions" are defined in terms of the strength and anisotropy in $\Delta W_3(r,\theta)$. In our polymer-grafted NPs, we expect $\Delta W_3(r,\theta)$ to arise from the expulsion of polymer grafts from in between the two dimer NPs.

We aim to compute and analyze the distance- and orientation-dependent behavior of the overall PMF $W(r,\theta)$ as well as its three-body contribution $\Delta W_3(r,\theta)$. The first quantity provides a measure of the overall free energy of the three-particle system and helps determine the stability of the various assembled configurations of the system, both isotropic and anisotropic. The latter quantity provides a measure of the "anisotropicity" in the interactions between the test NP and the NP-dimer and its underlying source. However, traversing such a two-dimensional coordinate space in r and θ would entail prohibitive computational costs. To this end, we computed the PMF along four representative "reaction coordinates" spanning the relevant angular space around one of the dimer NPs (Figure 1c): (1) longitudinal axis of the NP-dimer (denoted by $\mathbf{x}_{0^\circ}$), (2) tilted axis oriented 45° with respect to the longitudinal axis denoted by ($\mathbf{x}_{45^\circ}$), (3) perpendicular axis oriented 90° with respect to the longitudinal axis denoted by ($\mathbf{x}_{90^\circ}$), and (4) different perpendicular axis that passes through the dimer center of mass rather than through the NP center ($\mathbf{x}'_{90^\circ}$). The PMFs were obtained as a function of the surface-to-surface distance d between the cores of the test NP and the closest dimer NP and *not* the center-to-center distance as typically used. For comparison, we also computed "two-particle" PMF between a test NP and an isolated or "reference" NP also as a function of their surface-to-surface distance d (Figure 1d).

Coarse-Grained Model. To compute the PMFs between polymer-grafted NPs in a polymer matrix, we adopted a coarse-grained model (Figure 2a) similar to one we previously used for investigating the viscoelastic properties of polymer−nanoparticle composites.[23] The model is simple as well as computationally efficient and captures the essential physics of free and grafted polymer chains and the interactions between NP cores.

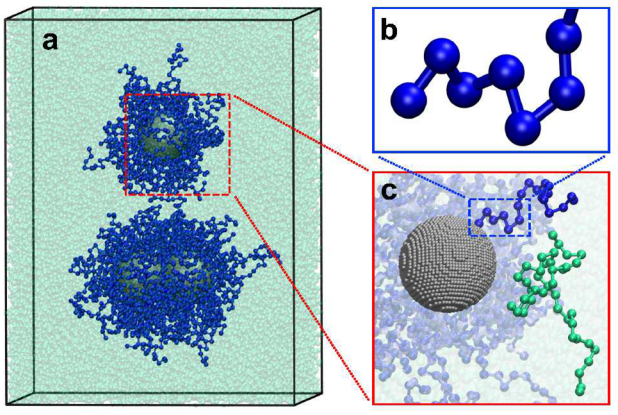

Figure 2. (a) Schematic of the simulation setup used for computing three-particle PMFs between polymer-grafted NPs within a polymer matrix. (b, c) Grafted polymer chains (blue) and matrix chains (green) are treated as coarse-grained bead−chains. NP cores (gray) are treated as spheres constructed from a rigid simple-cubic lattice of atoms.

According to this model, segments of the grafted and matrix polymer chains were treated as beads of size σ and mass m (Figure 2b).[24] Adjacent segments in each chain were connected by a finitely extensible nonlinear elastic (FENE) spring with potential energy given by

$$U_{\mathrm{FENE}} = -\frac{k}{2}R_0^{\,2}\ln\left[1-\left(\frac{r}{R_0}\right)^2\right] \tag{1}$$

where r is the separation distance between the bonded segments, $R_0 = 1.5\sigma$ is the maximum possible length of the spring, $k = 30\epsilon/\sigma^2$ is the spring constant, and ϵ is the characteristic energy parameter of the system. The above choice of parameters ensures that chains do not cross each other. Excluded volume interactions between all pairs of polymer segments, bonded or nonbonded, were treated using a short-range, purely repulsive potential[25]

$$U_{\mathrm{ev}} = \begin{cases} 4\epsilon\left[\left(\frac{\sigma}{r}\right)^{12} - \left(\frac{\sigma}{r}\right)^{6} + \frac{1}{4}\right] & r \le 2^{1/6}\sigma \\ 0 & r > 2^{1/6}\sigma \end{cases} \tag{2}$$

where r is the distance between the segments. While highly simplified, this polymer model captures well various experimentally measured structural and dynamical properties of simple polymeric melts spanning the Rouse and reptation regimes, including the chain-length dependence of the diffusion coefficient and the relaxation of the structure factor.[24] In this study, we examined graft chains of lengths L_g (in terms of number of segments) in the range 5−20 and matrix chains of lengths L_m in the range 1−40 segments. Apart from possible differences in their lengths, the grafted and matrix chains were considered to be chemically identical; that is, their segments exhibit identical interactions.

The NP cores were treated as spheres of diameter $D_c = 6\sigma$ constructed out of a rigid simple cubic lattice of "atoms" (Figure 2c). The total van der Waals (vdW) interactions between two NP cores was then calculated as the sum of individual vdW interactions between pairs of atoms *across* the two NP cores with each interaction treated using the Lennard-Jones (LJ) potential

$$U_{\mathrm{LJ}} = 4\epsilon_c\left[\left(\frac{\sigma_c}{r}\right)^{12} - \left(\frac{\sigma_c}{r}\right)^{6}\right] \tag{3}$$

where r is the distance between the interacting atoms and σ_c and ϵ_c are the atomic size and energy parameters, respectively. Such atom-level treatment of NP cores allows us to accurately capture the variation in the vdW interactions between NPs as a function of their separation distance; note that an analytical expression for such interactions between spheres is available for only very short or very large distances. The precise values of the lattice constant and atom size are not important as long as they are sufficiently small to minimize discretization (faceting) effects. We found that lattice constant λ and atom size σ_c set equal to 0.35σ yielded reasonably isotropic energies, with less than 10% variation in the total vdW energy across different

DOI: 10.1021/acs.macromol.6b01936
Macromolecules XXXX, XXX, XXX−XXX

orientations of the NP cores. The strength of vdW interactions can also be conveniently tuned by varying the value of ϵ_c. To calculate the surface-to-surface distance d between NP cores, we define their "surface" as the smallest spherical surface that encloses all their atoms, accounting for their vdW radii σ_c. Because the NP cores are rigid and near-isotropic, the interaction potential energy between two NP cores is a function of only their surface-to-surface separation distance. The potential energy profile therefore needs to be computed and tabulated just once before the MD simulations, which allowed us to avoid the use of a LJ cutoff that is typically employed in simulations.

The grafted chains were attached to the surface of each NP core also using FENE springs (eq 1). The grafting points were generated at the desired grafting density Γ_g using an algorithm[26,27] that yields a pseudouniform distribution of points on the surface of each NP core. The grafting points were treated as virtual beads and held fixed relative to each other and to their NP core center by using rigid body constraints. Excluded volume interactions between NP cores and the polymer segments were also treated via a short-range, purely repulsive potential

$$U_{\text{shift-LJ}} = \begin{cases} 4\epsilon\left[\left(\frac{\sigma}{r - r_{ev}}\right)^{12} - \left(\frac{\sigma}{r - r_{ev}}\right)^{6} + \frac{1}{4}\right] & r - r_{ev} \le 2^{1/6}\sigma \\ 0 & r - r_{ev} > 2^{1/6}\sigma \end{cases} \quad (4)$$

where r is the distance between the centers of the interacting NP and the polymer segments and the distance shift of $r_{ev} = (D_c - \sigma)/2$ ensured that the polymer segments and NP cores did not penetrate each other.

All simulation parameters and quantities are henceforth reported in units of σ, m, and ϵ, which set the length, mass, and time scales, respectively.

Potential of Mean Force Calculations. The PMFs along each of the four reaction coordinates shown in Figure 1c were computed using the so-called "blue moon ensemble" method.[28,29] This method involves the use of constrained MD simulations to confine a molecular system defined by atomic coordinates $\mathbf{r}^N$ to a subensemble in which the reaction coordinate $\xi(\mathbf{r}^N)$ is held fixed at a particular value ξ'. The PMF is calculated by thermodynamic integration of the "mean force" (the negative of the ensemble-averaged gradient of the Hamiltonian with respect to the reaction coordinate) collected from multiple such simulations conducted at different fixed values of the reaction coordinate. Accordingly, we performed MD simulations of the polymer−NP system in which the centers of the dimer NPs were held fixed and the test NP was held fixed at different positions ξ' along the examined reaction coordinate. While calculation of this mean force can become tedious for reaction coordinates that depend in a complex, nonlinear manner with atom positions, the calculation is relatively straightforward in our systems, where it reduces to evaluating the time-average of the *component* of the true force $\mathbf{F}(\xi')$ experienced by the test NP from the reference NP or NP-dimer along the direction of the reaction coordinate, which we denote by $\langle F(\xi')\rangle$.[30,31] The mean forces obtained from simulations conducted at different values of ξ' were then be integrated to obtain the PMF at any position d along the reaction coordinate:

$$W(d) = W(d_0) - \int_{d_0}^{d} \langle F(\xi')\rangle \, d\xi' \quad (5)$$

where $W(d_0)$ is the value of the PMF value at some reference point d_0 on the reaction coordinate. Choosing d_0 to be a sufficiently large distance ensures that the test NP does not interact with the NP-dimer whereupon $W(d_0) \approx 0$. We refer to the above PMF involving three NPs as "three-particle" PMFs. A similar approach was used for computing "two-particle" PMF between a test NP and an isolated or "reference" NP as a function of their surface-to-surface distance d (Figure 1d). To characterize the degree of anisotropy in these interactions, we also computed the three-body contribution to the overall three-particle PMFs via

$$\Delta W_3(d) = W(d) - W_2(d) - W_2(d') \quad (6)$$

where $W_2(d)$ and $W_2(d')$ are the values of the two-particle PMFs computed at the separation distances d and d' of the test NP from each of the two dimer NPs.

We also dissected the overall PMF into six different contributions arising from the interaction between: NP-dimer cores and test-NP core $[W_{c\to c}(d)]$; NP-dimer grafts and test-NP core $[W_{g\to c}(d)]$; NP-dimer cores and test-NP grafts $[W_{c\to g}(d)]$; NP-dimer grafts and test-NP grafts $[W_{g\to g}(d)]$; polymer matrix and test-NP core $[W_{m\to c}(d)]$; and matrix and test-NP grafts $[W_{m\to g}(d)]$. Each of these contributions was also computed via eq 5, by replacing the net force $\langle F(\xi')\rangle$ with the force component corresponding to the interaction being probed. Note that all components of the PMF *except* $W_{c-c}(d)$ involve some type of polymer-mediated interaction. Therefore, we can categorize the total PMF into a NP core-mediated component, which we denote as $W_c(d) \equiv W_{c-c}(d)$, and a polymer-mediated component, which we denote as $W_p(d) \equiv W_{g\to c}(d) + W_{c\to g}(d) + W_{g\to g}(d) + W_{m\to c}(d) + W_{m\to g}(d)$. Note that $W_c(d)$ is simply equal to $U_{vdW}(d)$, the total vdW interactions between the atoms of the interacting NP cores.

In all three-particle PMF calculations, the dimer NPs were held fixed with their cores contacting each other, and they were not allowed to relax to their equilibrium separation distance while the test NP was brought closer to the dimer along a reaction coordinate. This allowed us to maintain a fixed reference configuration of the NP-dimer, thereby ensuring that all variations in the PMFs observed with respect to the different parameters investigated here can be attributed solely to variations in the graft conformations with respect to these parameters and not to changes in the internal configuration of the dimer itself. Also, allowing for variations in the dimer configuration would amount to computing two-dimensional PMFs, as a function of the separation distance between the dimer NPs in addition to the position ξ' of the test NP along the reaction coordinate, which would increase the computational cost by an order of magnitude. As we demonstrate later, grafted NPs that assemble into stable dimers in this study do so with their cores almost touching each other. Hence, the PMFs computed with relaxed dimers resemble quite closely those computed using fixed dimers.

Molecular Dynamics Simulations. The MD simulations were carried out in the canonical ensemble using a rectangular simulation box employing periodic boundary conditions in all three directions. The box dimensions were taken to be large

DOI: 10.1021/acs.macromol.6b01936
Macromolecules XXXX, XXX, XXX−XXX

Table 1. Details of Simulation Systems Examined in This Study

system no.[a]	L_g[b]	L_m[c]	Γ_g[d]	n_g[e]	n_m[f,h]	V[g,h]
			reference system			
1[i]	20	40	0.4	45	916, 1011, 1080	47216, 52949, 56315
			effect of polymer grafts			
1	20	40	0.4	45	916, 1011, 1080	47216, 52949, 56315
2	10	40	0.4	45	418, 471, 520	21714, 24961, 27351
3	5	40	0.4	45	138, 156, 192	7507, 8772, 10528
4	20	40	0.2	23	938, 1044, 1112	47104, 52949, 56266
5	10	40	0.2	23	430, 486, 540	21763, 24888, 27522
6	5	40	0.2	23	142, 165, 200	7434, 8809, 10516
7	20	40	0.1	11	950, 1065, 1136	47104, 53095, 56559
8	10	40	0.1	11	436, 495, 548	21763, 24888, 27473
9	5	40	0.1	11	146, 171, 204	7482, 8882, 10492
			effect of polymer matrix			
1	20	40	0.4	45	916, 1011, 1080	47216, 52949, 56315
10	20	20	0.4	45	1832, 2022, 2160	47216, 52949, 56315
11	20	5	0.4	45	7328, 8088, 8640	47216, 52949, 56315
12	20	1	0.4	45	36640, 40440, 43200	47216, 52949, 56315
13	20	0	0.4	45	0, 0, 0	47216, 52949, 56315

[a]Index identifying the simulation system from a total of 13 studied systems. [b]Length of grafted chains. [c]Length of matrix chains. [d]Grafting density. [e]Number of grafted chains per NP. [f]Number of matrix chains in simulation box. [g]Volume of simulation box. [h]Values correspond to simulations used for computing PMFs along 2- and 3-particle ($\mathbf{x}_{0^\circ}$, $\mathbf{x}_{90^\circ}$) reaction coordinates; values used for computing PMFs along $\mathbf{x}'_{90^\circ}$ are identical to those along $\mathbf{x}_{90^\circ}$. [i]For this reference system we computed the PMF along an additional reaction coordinate ($\mathbf{x}_{45^\circ}$) for which we employed n_m = 1119 and V = 58 189.

enough to accommodate the polymer-grafted NPs in their most spread-out configuration for the PMF calculation along each reaction coordinate; this was achieved by employing a padding of at least 2.5σ along the six directions. The NP-polymer system was simulated in a meltlike state with a density of $\rho_p \equiv n_b/V_b$ = 0.82, where n_b is the total number of grafted and matrix chain segments and V_b is the volume available to these segments, i.e., volume of the simulation box minus the volume of the NP cores. The equations of motion were integrated by using a velocity-Verlet algorithm with a time step of Δt = 0.002. A Nosé−Hoover thermostat[32] with a time constant of τ = 1 was used for maintaining the temperature at T = 1 (in units of ϵ/k_B), though it should be noted that our polymer chains are largely athermal. All simulations were performed using the LAMMPS package developed by Sandia National Laboratories.[33]

The simulations were initialized by placing the grafted NPs and the polymer chains in a simulation box 50−100 times larger than the required dimensions to prevent overlap among the chain segments and NP cores. The box was then gradually compressed in each direction until the targeted box dimension or polymer density was reached. Next, the NPs were assembled into a configuration used for initiating the PMF calculations: We slowly moved two of the NPs into the dimer configuration with their cores touching each other, i.e., their centers are D_c apart (Figures 1 and 2), and simultaneously moved the third NP to a distance $d = d_0 \equiv 12$ along the reaction coordinate being probed, a separation distance large enough to prevent the NP from interacting with the dimer. This initialization procedure was carried out over a period of 0.2−0.5 million time steps. Thereafter, the centers of the dimer NPs were held fixed.

To compute the PMF profile, the center of the test NP was moved in a stepwise manner along the reaction coordinate toward the NP-dimer, first at steps of $\Delta\xi'$ = 1 until a distance of ξ' = 4 was reached and then at steps of $\Delta\xi'$ = 0.25 until contact. During the mobile phase of each step, the NP center was moved at a velocity of 0.000 01σ per time step until the target $\Delta\xi'$ was reached. The NP center was held fixed for a time period of 0.6 million time steps during the stationary phase of each step. The ensemble-averaged force $\langle F(\xi')\rangle$ and the ensemble-averaged components of the force experienced by the test NP were computed from the last 0.5 million time steps of this stationary phase. The test NP and the dimer NPs were allowed to rotate throughout the simulations. The simulations along each reaction coordinate were repeated four times to improve accuracy and facilitate the calculation of error bars. A similar procedure was used for calculating the two-particle PMFs. The NP centers were fixed or moved using "hard" restraints implemented through the "fix move" command in LAMMPS; particles restrained in this manner are no longer influenced by forces from adjacent particles or from the thermostat.

Since the atomic lattice comprising the cores of the test and dimer NPs and their centers are also held fixed using hard restraints in each MD simulation at fixed distance ξ', the net vdW interaction energy $U_{vdW}(\xi')$, or vdW force $F_{vdW}(\xi')$, between the cores remains fixed during each such simulation. This feature allows for significant computational savings because the vdW portion of the PMF $W_c(d) \equiv U_{vdW}(d)$ can be calculated separately just once before or after the simulation via eq 3; $W_c(d)$ can then be added back onto the portion of PMF $W_p(d)$ arising from polymer-mediated forces that fluctuate during the simulations at fixed ξ' to yield the overall PMF $W(d)$. Furthermore, since the computed $U_{vdW}(d) \propto \epsilon_c$, one can calculate it for the reference ϵ_c = 1 to yield a reference $U^0_{vdW}(d)$, which can then be used to obtain $U_{vdW}(d)$ for any arbitrary value of ϵ_c via $U_{vdW}(d) = \epsilon_c \times U_{vdW}(d)$. This allows us to explore arbitrary strengths of core/core interaction without actually performing simulations at each of those ϵ_c values.

Systems and Parameters Investigated. To explore how NP interactions are affected by various attributes of the grafted

DOI: 10.1021/acs.macromol.6b01936
Macromolecules XXXX, XXX, XXX−XXX

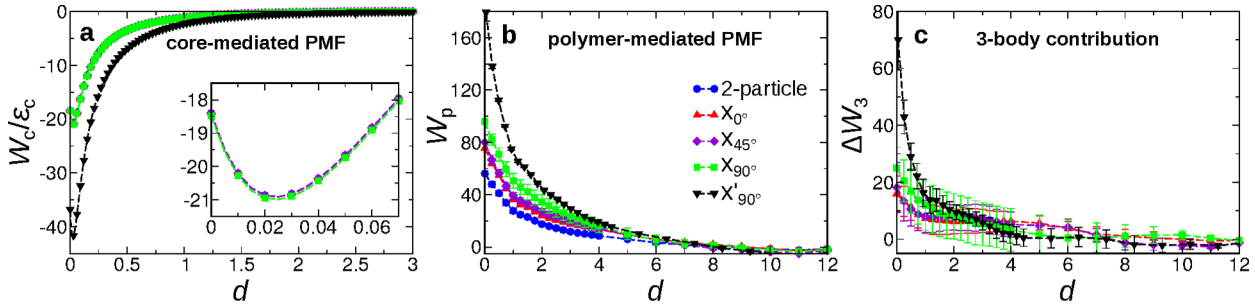

Figure 3. (a, b) Core and polymer-mediated components of the overall PMF computed along the two- and three-particle reaction coordinates for the representative NP−polymer system with L_g = 20, Γ_g = 0.4, and L_m = 40. (a) Core-mediated component normalized by interatomic energy parameter ϵ_c. Inset shows close-up of the profiles at small d. (b) Polymer-mediated component. (c) Three-body contribution to the overall PMF.

NPs and the polymer matrix, we computed the PMFs for a range of NP−polymer systems listed in Table 1. To keep the number of systems investigated to a manageable amount, the NP core diameter was fixed at D_c = 6 and the interactions mediated by the grafts and matrix chains were fixed according to eqs 1−4. The former ensures that the NPs are much larger than the polymer segments, consistent with most experimental systems, and the latter ensures that the grafted and matrix polymer are chemically identical and that they interact with each other and with the NP cores via excluded volume interactions. We explored the effect of four parameters considered to affect the morphology of self-assembled NP structures:[22]

- *Matrix chain length*. Four different values were examined: L_m = 1, 5, 20, and 40 (note that value 1 corresponds to a "monomeric" solvent), yielding chain radii of gyration of R_g = 0.5, 1.12, 2.15, and 3.15. This allowed us to probe four different NP-to-matrix size ratios $D_c/2R_g$ = 0.95, 1.4, 2.7, and 6 without altering NP size. This size ratio is known to affect the morphology of NP structures, with larger values leading to higher-dimensional structures, and is therefore also expected to affect NP/NP interactions. We *also* examined the impact of complete removal of matrix chains, that is polymer-grafted NPs interacting in a vacuum.
- *Graft chain length*. Three different chain lengths L_g = 5, 10, and 20 were examined, which together with variations in the grafting density described below allow us to explore a wide range of grafting regimes known to affect the interactions between polymer-grafted NPs.
- *Grafting density*. Three different values Γ_g = 0.1, 0.2, and 0.4 were examined. To characterize the conformation of the grafts, we computed the dimensionless surface coverage parameter $\Gamma_g^* \equiv \Gamma_g R_g^{*2}$, where R_g^* is the unperturbed radius of gyration of the grafts (free chains not grafted to NP surface).[23] Our calculations indicate that we explored conformations ranging from the mushroom regime (Γ_g^* = 0.1) to the dilute brush regime (Γ_g^* = 1.85).
- *NP core/core interaction strength*. This is dictated solely by the magnitude of the energy parameter ϵ_c. As explained earlier, we can explore potentially any arbitrary value of ϵ_c for every combination of L_m, L_g, and Γ_g investigated here (Table 1) without performing any additional simulations. In general, we considered values of ϵ_c in the range 0.5−3 that allowed us explore both stable and unstable configurations of associated NP clusters.

In all systems studied here, the grafted and matrix polymer chains are chemically identical and modeled using FENE bonds and short-ranged, purely repulsive nonbonded interactions. In this study, we refrained from exploring attractive nonbonded interactions and also studying systems with chemically different NP-grafts and matrix chains. Examining such effects would entail significantly higher computational costs, not only due to the slower conformational sampling of attractive systems via MD simulations but also due to the introduction of additional parameters in the system associated with graft−graft, graft−matrix, and matrix−matrix interactions. It was recently shown that replacing the repulsive nonbonded potential in the above model with an attractive Lennard-Jones potential had negligible effect on the structure and dynamics of polymer chains simulated at meltlike densities and temperatures at least twice as large as the glass transition temperature, T_g.[34] Thus, we do *not* expect the introduction of uniformly attractive interactions across grafted and matrix polymer chains to have any significant effect on computed PMFs given that we performed our simulations in the melt phase at $T = \epsilon/k_B$, much higher than T_g ($\sim 0.4\epsilon/k_B$). However, differences in interactions among and between grafts and matrix chains should affect the PMFs; for instance, if the matrix−graft interactions were attractive while the graft−graft and matrix−matrix interactions were repulsive, then one would expect the grafted-NPs to exhibit less attraction (or more repulsion) with each other as compared to systems with chemically identical grafts and matrix chains.

RESULTS AND DISCUSSION

Anisotropy in NP Interactions. To determine if and how the interactions between two polymer-grafted NPs become anisotropic when a third NP is in close proximity to one of the NPs, we computed using molecular dynamics (MD) simulations the potential of mean force (PMF) between a test NP and a NP-dimer along four distinct reaction coordinates spanning the angular space around the dimer. Though we computed such PMFs for a range of NP-polymer systems, we present below results computed for one representative system comprising of NPs grafted with polymer chains of length L_m = 40 at a grafting density of Γ_g = 0.4 surrounded by a polymer matrix of chain length L_g = 20 (Table 1, system 1). As discussed later, this system with long and dense NP-grafts displays strong anisotropic interactions, making it an ideal system for showcasing this phenomenon and elucidating its physical basis.

Figures 3a and 3b show the core- and polymer-mediated components $W_c(d)$ and $W_p(d)$ of the overall PMF computed along the four chosen reaction coordinates. For comparison, we also plot for the same system the two components of the two-

DOI: 10.1021/acs.macromol.6b01936
Macromolecules XXXX, XXX, XXX−XXX

particle PMF. The core-mediated component $W_c(d)$ scales linearly with the LJ energy parameter ϵ_c of the NP-core atoms and is thus plotted in units of ϵ_c (Figure 3a). As expected, this component is always attractive for distances $d > 0$ where all core atoms interacting across the test and dimer NPs are separated by a distance greater than σ_c. At smaller distances $d < 0$, some of these atoms begin to overlap and W_c rises and becomes repulsive. All $W_c(d)$ exhibit a minimum close to contact, at roughly $d = 0.024\sigma$, which is consistent with the notion that the NP cores can further lower their vdW energy by getting closer than $d = (2^{1/6} - 1)\sigma_c \equiv 0.043\sigma$ (location of the energy minimum for the interaction between the closest pair of atoms on different cores directly facing each other) to increase favorable interactions between the remaining atoms of the interacting cores. The three-particle $W_c(d)$ profiles along all reaction coordinates *except* $\mathbf{x}'_{90°}$ are almost identical to the profile obtained for the two-particle configuration. The reason is that the LJ interaction between the NP-core atoms is short-ranged, and none of these reaction coordinates allow the test NP to simultaneously contact both NPs of the dimer. Each of these profiles exhibits an attractive well whose depth scales as $\approx 21\epsilon_c$. The $W_c(d)$ profile along $\mathbf{x}'_{90°}$ is exactly twice in magnitude to that of the two-particle PMF given that the test NP now feels exactly the same attraction from both NPs of the dimer, which also implies that the three-body contribution ΔW_3 is exactly zero, as expected for rigid cores. Also as expected, the three-body contribution to the $W_c(d)$ for the remaining three profiles is zero as well.

The polymer-mediated PMF components $W_p(d)$, on the other hand, are all repulsive and decrease much slower than $W_c(d)$ with increasing separation distance d (Figure 3b). By $d \sim 7-8$, the polymer grafts of the interacting NPs are out of reach of each other and W_p approaches zero. Importantly, the $W_p(d)$ profiles for the three-particle PMFs are substantially more repulsive than that of the two-particle PMF. More importantly, the polymer-mediated repulsion displays large variation across the four reaction coordinates. In particular, the degree of repulsion increases in the order $\mathbf{x}_{0°} < \mathbf{x}_{45°} < \mathbf{x}_{90°} < \mathbf{x}'_{90°}$. Thus, while $W_c(d)$ is largely independent of the orientation of the test NP with respect to the NP-dimer, except for the sharp enhancement close to the perpendicular axis of the dimer, $W_p(d)$ shows a more uniform increase with the orientation angle away from the poles of the NP-dimer.

In Figure 3c, we have plotted the three-body contribution ΔW_3 to the overall PMF, which arises completely from polymer-mediated interactions, as the core-mediated PMF does not have any three-body contribution. We find that ΔW_3 is substantial and contributes 30−40% of the overall polymer-mediated repulsion (W_p) at near-contact $d \approx 0$, and as expected, this contribution becomes smaller with further distance. Furthermore, ΔW_3 increases in the order $\mathbf{x}_{0°} < \mathbf{x}_{45°} < \mathbf{x}_{90°} < \mathbf{x}'_{90°}$ with respect to the four reaction coordinates; i.e., the three-body contribution becomes larger as the test NP moves from the pole of the dimer ($\theta = 0$) to the contact point of the two dimer NPs ($\theta \approx 4\pi/3$; see Figure 1a).

Figure 4 shows the overall three-particle PMF $W(d)$ for two representative values of the energy parameter ($\epsilon_c = 3$ and 7) depicting intermediate and strong core−core attraction. Note that for much smaller or much larger values of ϵ_c, $W(d)$ converge to $W_p(d)$ and $W_c(d)$, respectively. Compared to the two components, the overall PMFs exhibit a more complex dependence with distance and reaction coordinate. First, for sufficiently strong core/core attraction, the overall PMFs

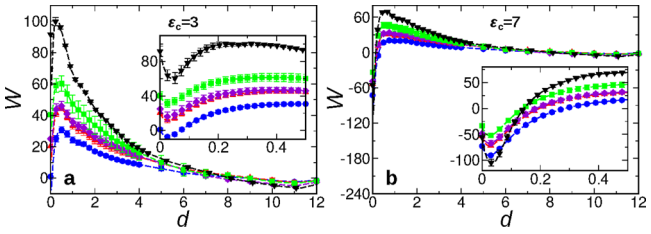

Figure 4. Overall PMFs computed along the two- and three-particle reaction coordinates for the representative NP−polymer system with $L_g = 20$, $\Gamma_g = 0.4$, and $L_m = 40$. The PMFs have been computed for (a) $\epsilon_c = 3$ and (b) $\epsilon_c = 7$. Insets show close-ups at small d. Figure legends same as in Figure 3.

exhibit an energy barrier at short distances, which separates the stable (or metastable) bound state of the test NP from its dispersed state. The height of this energy barrier depends on the strength of the core−core attraction. Second, the overall PMFs no longer necessarily exhibit monotonic variations in the strength of attraction (or repulsion) with orientation as exhibited by $W_p(d)$ and $W_c(d)$. For example, the most stable bound state of the test NP occurs along the $\mathbf{x}'_{90°}$ coordinate when $\epsilon_c = 7$, whereas it occurs along $\mathbf{x}_{0°}$ when $\epsilon_c = 3$. Indeed, it is such variations in the relative stability of the different bound states of NPs that leads to the rich and complex phase behavior exhibited by polymer-grafted NPs, as discussed in more detail further below. Interestingly, all PMFs $W(d)$ that exhibit an energy minimum do so at a distance close to the location of the minimum exhibited by the core-mediated PMF $W_c(d)$. This observation is not surprising given the sharp, shorter-ranged decay of the vdW core/core attraction as compared to the flatter, longer-ranged decay of polymer-mediated repulsion, which causes the cores to position themselves close to each other to take advantage of the strong vdW attraction without sacrificing much steric repulsion.

The overall PMFs also importantly reveal that the dimer NPs prefer to assemble with their cores almost touching each other ($d \approx 0.024\sigma$), very similar to the contact configuration ($d = 0$) we used for computing three-particle PMFs. Given that this difference in the dimer configuration is much smaller than even the size of a single polymer segment (σ), we expect the three-particle PMFs computed here to closely approximate the "true" three-particle PMFs obtained from calculations in which the dimers are allowed to relax. To confirm this, we conducted additional simulations to compute the three-particle $W_p(d)$ with dimer NPs separated by 0.024σ. Our results plotted in Figure S1 showed that the PMFs are indeed very close to each other.

Monomer Density Distribution. It was previously proposed[17,18,22] that the anisotropic assembly of spherical grafted NPs could putatively arise from the displacement of polymer grafts from in between the interacting NPs, potentially leading to anisotropic distribution of polymer chains around the NPs. To investigate if the observed anisotropy in the overall polymer-mediated repulsion $W_p(d)$ and in its three-body contribution $\Delta W_3(d)$ (Figure 3b,c) is related to any such changes in polymer density, we computed the position-dependent segmental density around a NP-dimer, defined here as the number of polymer chain segments (beads) per unit volume. For this purpose, we carried out separate MD simulations of the NP-dimer in the same polymer matrix, *but* without the test NP, and computed three kinds of densities: the *overall* segmental density $\rho_{g+m}(x,r)$ (Figure 5a) arising from

DOI: 10.1021/acs.macromol.6b01936
Macromolecules XXXX, XXX, XXX−XXX

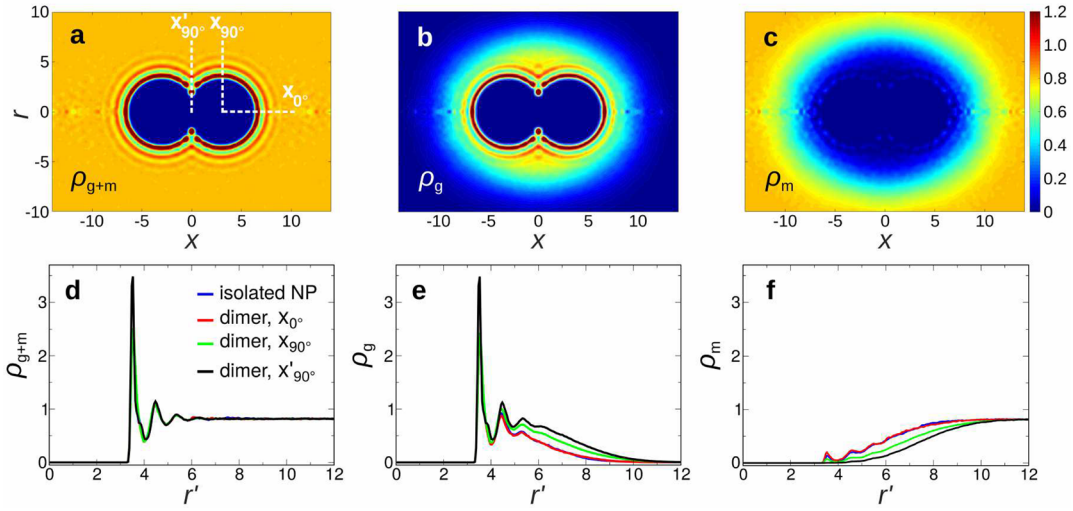

Figure 5. 2D contour maps of (a) overall segmental density $\rho_{g+m}(x,r)$, (b) graft segmental density $\rho_g(x,r)$, and (c) matrix segmental density $\rho_m(x,r)$ surrounding the NP-dimer. Color bars denote the density magnitude in units of segments/σ^3. (d) Overall segmental density $\rho_{g+m}(r')$, (e) graft segmental density $\rho_g(r')$, and (f) matrix segmental density $\rho_g(r')$ profiles along the three reaction coordinates labeled in (a) plotted as a function of radial distance r' from the center of the dimer NP. The "reference" density profile around an isolated NP as a function of radial distance from its center is shown in blue.

both grafted and matrix chains, the *graft* segmental density $\rho_g(x,r)$ (Figure 5b) arising from grafted chains alone, and the *matrix* segmental density $\rho_m(x,r)$ (Figure 5c) arising from matrix chains alone, each of which were computed as a function of the longitudinal (x) and radial coordinate (r) relative to the NP-dimer. To more directly relate these densities to the computed $W_p(d)$ and $\Delta W_3(d)$, we also obtained 1D segmental density profiles $\rho_{g+m}(r')$ (Figure 5d), $\rho_g(r')$ (Figure 5e), and $\rho_m(r')$ (Figure 5f) as a function of the radial distance r' to the center of the dimer NP(s) along the reaction coordinates introduced earlier. Because W_p (and ΔW_3) and the density profile along $\mathbf{x}_{45°}$ are only marginally different from that along $\mathbf{x}_{0°}$, we present only the density profiles along the three reaction coordinates $\mathbf{x}_{0°}$, $\mathbf{x}_{90°}$, and $\mathbf{x}'_{90°}$. For comparison, we also computed the density profile around a single NP as a function of radial distance r' from its center, as computed from a separate MD simulation of an isolated NP in a polymer matrix.

The overall segmental density shows enhancement and oscillations close to the surface of the dimer (Figure 5a) that are more apparent in the $\rho_{g+m}(r')$ profiles (Figure 5d). This behavior is caused by a combination of two effects: the tethering of the terminal graft segment to the NP core and the layering of particles (segments) with excluded volume next to an impenetrable wall (NP cores). Sufficiently far from the dimer surface (>3σ), the densities asymptote to the bulk density. More importantly, we observe minimal variations in $\rho_{g+m}(x,r)$ around the two dimer NPs with respect to the angular coordinate. In particular, $\rho_{g+m}(r')$ profiles along the three reaction coordinates $\mathbf{x}_{0°}$, $\mathbf{x}_{90°}$, and $\mathbf{x}'_{90°}$ all remain similar to the density profile obtained for the isolated NP. These results indicate that the observed anisotropy in polymer-mediated repulsion between NPs might *not* arise from any enhancement in the overall segmental density near the contact region of the dimer.

The segmental density associated with grafts only, in contrast, displays strong anisotropy, as noted from the angle dependence of $\rho_g(x,r)$ (Figure 5b) or from differences in $\rho_g(r')$ across the three reaction coordinates (Figure 5e). In particular, the region around the dimer that displays high to moderate density ($\rho_g \gtrsim 0.4$), as depicted by the green−cyan halo in Figure 5b, extends farther into the matrix along the perpendicular than the longitudinal coordinate. The $\rho_g(r')$ profiles show that the density rises monotonically from the dimer poles to the contact region, i.e., in the order $\mathbf{x}_{0°} < \mathbf{x}_{90°} < \mathbf{x}'_{90°}$ (Figure 5e). These results suggest that when two NPs come into contact, as in the case of the dimer, their intervening grafts get pushed outward into the region immediately surrounding the contact point, causing a strong enhancement in the graft segmental density along the perpendicular axis passing through the contact point. The displaced grafts encroach on their neighboring grafts, causing them to extend outward and sideways, triggering a "domino effect" that propagates outward from the contact point to the dimer poles. That the density along $\mathbf{x}_{0°}$ is only slightly higher than that for a single NP (Figure 5e) indicates that the propagation eventually subsides, with the grafts at either of the two dimer poles remaining mostly unaffected by the presence of the other dimer NP. We also observe that the $\rho_g(r')$ profiles along the three reaction coordinates increase in the same sequence as the three-particle $W_p(d)$ profiles and that the $\rho_g(r')$ profile along $\mathbf{x}_{0°}$ is only slightly higher than its two-particle counterpart, also similar to $W_p(d)$ (see Figure 3b). This close analogy between $W_p(d)$ and $\rho_g(r')$ suggests that the anisotropy in polymer-mediated PMFs may be caused by the anisotropy in the graft segmental density, thereby providing direct support for the hypothesis that the anisotropic interactions between NPs could indeed arise from the conformational rearrangement of grafted chains at the contact region.

Lastly, the segmental density arising from the matrix chains shows the opposite trends compared to those exhibited by the density arising from the grafts. In this case, $\rho_m(x,r)$ gets increasingly depleted as one gets closer to the dimer surface, evidently due to increased exclusion by the polymer grafts. Also, the depletion of matrix chains is most severe along $\mathbf{x}'_{90°}$ and gets weaker as one rotates toward the dimer axis, the $\mathbf{x}_{0°}$ coordinate. As discussed below, this anisotropy in the depletion of matrix chains around the dimer will lead to an anisotropy in the depletion forces between test NP and the dimer.

DOI: 10.1021/acs.macromol.6b01936
Macromolecules XXXX, XXX, XXX−XXX

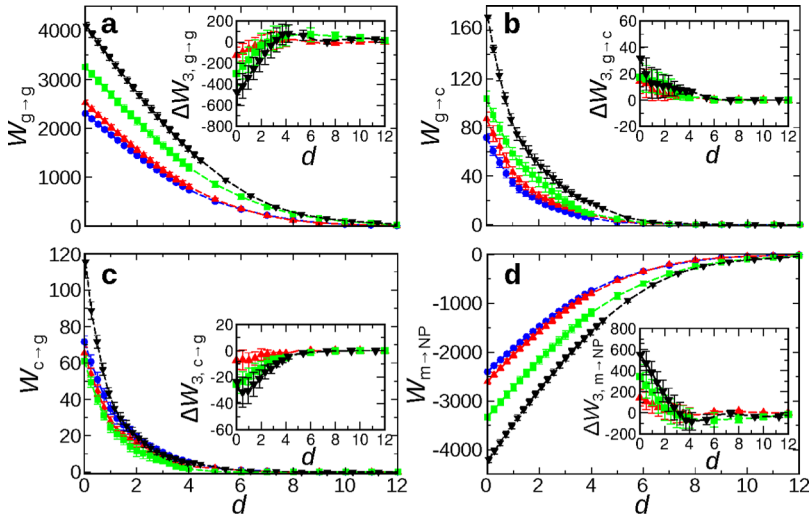

Figure 6. Breakdown of the net polymer-mediated repulsion W_p into its four components: (a) $W_{g\to g}$, (b) $W_{g\to c}$, (c) $W_{c\to g}$, and (d) $W_{m\to NP}$. Each component is plotted as a function of position d along the two- and three-particle reaction coordinates. The insets provide the three-body contributions for each of these components.

Steric versus Depletion Interactions. Polymer-mediated interactions between grafted NPs in a polymeric matrix arise from a combination of steric repulsion due to compression of the grafted chains and depletion attraction due to osmotic pressure of the matrix chains. To evaluate the role of steric and depletion forces in producing the anisotropic polymer-mediated repulsion between NPs, we dissected $W_p(d)$ into components arising from the interactions between (1) NP-dimer grafts and test-NP grafts, $W_{g\to g}(d)$; (2) dimer cores and test-NP grafts, $W_{c\to g}(d)$; (3) dimer grafts and test-NP core $W_{g\to c}(d)$; (4) polymer matrix and test-NP grafts $W_{m\to g}(d)$; and (5) polymer matrix and test-NP core $W_{m\to c}(d)$. The first three components involving the polymer grafts of the test or dimer NPs constitute "steric" interactions, while the last two components arising from the polymer matrix constitute "depletion" interactions.

We begin by examining how these individual components vary with respect to the reaction coordinate. Incidentally, the computed $W_{m\to c}(d)$ were substantially smaller than $W_{m\to g}(d)$ and had a large statistical uncertainty, which made it difficult to glean any statistically significant trends. To this end, we combined both these matrix-centered terms into a single term that we denote by $W_{m\to NP}(d)$ corresponding to the net depletion force acting on the *entire* test NP. Figure 6 shows the four components $W_{g\to g}(d)$, $W_{c\to g}(d)$, $W_{g\to c}(d)$, and $W_{m\to NP}(d)$ corresponding to the two-particle PMF and the three-particle PMFs along $\mathbf{x}_{0°}$, $\mathbf{x}_{90°}$, and $\mathbf{x}'_{90°}$. The insets provide the three-body contributions $\Delta W_{3,g\to g}(d)$, $\Delta W_{3,g\to c}(d)$, $\Delta W_{3,c\to g}(d)$, and $\Delta W_{3,m\to NP}(d)$ for each of these four interactions along $\mathbf{x}_{0°}$, $\mathbf{x}_{90°}$, and $\mathbf{x}'_{90°}$.

The PMF component $W_{g\to g}(d)$ arising from graft−graft interactions (Figure 6a) is found to be extremely repulsive, approaching 1000s of k_BT at contact (d = 0). Decomposing $W_{g\to g}(d)$ further into its energetic and entropic contributions using an approach described elsewhere[31] (Figure S2) reveals that most of this repulsion arises from the huge entropic loss incurred by the grafts that get increasingly squeezed in between the NP cores as they approach each other. Furthermore, the repulsion is stronger for the three-particle configurations and increases in the order $\mathbf{x}'_{0°} < \mathbf{x}_{90°} < \mathbf{x}'_{90°}$, with the former approaching the two-particle $W_{g\to g}$. Clearly, the strong enhancement in graft segmental density along $\mathbf{x}'_{90°}$ (Figure 5b,e) is responsible for the strong graft−graft repulsion along this reaction coordinate. The smaller enhancements along $\mathbf{x}_{90°}$ and $\mathbf{x}_{0°}$ lead to concomitantly smaller degrees of repulsion along those reaction coordinates. Interestingly, the three-body contributions to graft−graft repulsion are all negative (attractive), suggesting that the cumulative graft−graft repulsion arising from the two dimer NPs in isolation is stronger than that arising from the dimer. This result is likely related to the cumulative graft segmental density arising from two isolated dimer NPs being much higher than that from the dimer (see Figure 5e), which, despite the anticipated stronger-than-linear dependence of steric repulsion with graft segmental density, leads to stronger graft/graft repulsion. In addition, the three-body contributions are found to become increasingly negative in the order $\mathbf{x}'_{0°}$, $\mathbf{x}_{90°}$, and $\mathbf{x}'_{90°}$.

The two components $W_{g\to c}(d)$ and $W_{c\to g}(d)$ arising from interactions between NP grafts and cores are also purely repulsive, but more than an order of magnitude weaker than $W_{g\to g}(d)$ due to the strong shielding of NP cores by their grafts (Figures 6b,c). Similar to $W_{g\to g}(d)$, the $W_{g\to c}(d)$ repulsion also increases in the order $\mathbf{x}_{0°} < \mathbf{x}_{90°} < \mathbf{x}'_{90°}$ with the repulsion along $\mathbf{x}_{0°}$ approaching that in the two-particle configuration. This trend is expected given that the graft segmental density around the dimer NPs also increases in the same sequence, leading to more interactions between the dimer grafts and the test NP core along the two perpendicular directions as compared to the longitudinal direction. However, $W_{c\to g}(d)$ exhibits a somewhat different trend in that the repulsion along $\mathbf{x}_{0°}$ is weaker than that for the two-particle configuration and becomes even weaker along $\mathbf{x}_{90°}$. The reason is that the increasing graft segmental density along $\mathbf{x}_{0°}$ and then $\mathbf{x}_{90°}$ shields the dimer NP core from interacting with the test NP grafts. Interestingly, the repulsion rises up again along $\mathbf{x}'_{90°}$ because both dimer cores are now able to interact with the grafts of the test-NP. The three-body contributions to $W_{g\to c}(d)$ are all positive. The positive contribution arises from the enforced interactions of polymer grafts from the dimer with the surface of the test NP core due to their inability to escape from the tight confinement in between the test and dimer NPs. Comparatively, polymer grafts from isolated dimer NPs have much more freedom to get

DOI: 10.1021/acs.macromol.6b01936
Macromolecules XXXX, XXX, XXX−XXX

displaced. In contrast, the three-body contributions to $W_{c\to g}(d)$ are all negative, which is likely due to the increased cumulative ability of test NP grafts to interact with the surface of the dimer NPs when isolated as compared to the dimer that excludes a large fraction of the dimer NPs from interacting with the grafts. As usual, the magnitude of the three-body terms for both these interactions increase in the order $\mathbf{x}_{0^\circ} < \mathbf{x}_{90^\circ} < \mathbf{x}'_{90^\circ}$.

The last component $W_{m\to NP}(d)$ due to depletion interactions is strongly attractive (Figure 6d). The main source of this attraction is the difference in the osmotic pressure that develops across the two halves of the test NP (facing toward and away from the dimer) due to exclusion of matrix chains from in between the test NP and the dimer. This component is so strong that it almost counterbalances the graft−graft repulsion. In addition, the magnitude of depletion attraction increases in the order $\mathbf{x}_{0^\circ} < \mathbf{x}_{90^\circ} < \mathbf{x}'_{90^\circ}$ with the former approaching the two-particle $W_{m\to NP}(d)$. This trend is consistent with that of the graft segmental density in the region in between the test and dimer NPs (Figure 5b,d), which rises in the same order with respect to the reaction coordinates, leading to increasing exclusion of the matrix chains from this region, and thereby higher depletion attraction. The three-body contributions to depletion attraction are all positive. This can be explained in terms of the overlap between the excluded volumes of the test NP and NP-dimer being smaller than the sum of the overlaps between the excluded volumes of the test NP and the dimer NPs individually. The magnitude of three-body contributions again increase in the order $\mathbf{x}'_{0^\circ}$, $\mathbf{x}_{90^\circ}$, and $\mathbf{x}'_{90^\circ}$.

The rise in polymer-mediated repulsion $W_p(d)$ with increased tilting of the reaction coordinate from the dimer longitudinal axis may now be explained in terms of a competition between the net steric repulsion $W_{ster} \equiv W_{g\to g} + W_{g\to c} + W_{c\to g}$ and depletion attraction $W_{depl} \equiv W_{m\to NP}$. Figure 7a compares the net steric repulsion against depletion attraction for the two- and three-particle configuration. While both interactions become stronger with increased tilting of the reaction coordinate, as explained above in terms of the gradient in the graft segmental density from dimer contact point to poles, the increase in steric repulsion always exceeds that in depletion attraction, causing an increased net repulsion with increased tilting of the reaction coordinate. A possible explanation for this observation is provided further below.

To further evaluate the contribution of the three components of steric repulsion $W_{g\to g}$, $W_{g\to c}$, and $W_{c\to g}$ to the increase in overall repulsion with tilting of the reaction coordinate, we calculated the difference $\Delta W_i|_j \equiv W_i(0)|_{3\text{-particle},j} - W_i(0)|_{2\text{-particle}}$ in the value of the four PMF components $i \equiv$ g → g, g → c, c → g, and m → NP *between* the three- and two-particle configurations. These differences were calculated for each of the three reaction coordinates $j \equiv \mathbf{x}_{0^\circ}$, $\mathbf{x}_{90^\circ}$, and $\mathbf{x}'_{90^\circ}$ at the contact distance $d = 0$, where the repulsion $W_p(d)$ is the strongest. This analysis, presented in Figure 7b, reveals that the stronger repulsion $W_p(d)$ along $\mathbf{x}_{0^\circ}$ (compared to the two-particle scenario) (Figure 3b) occurs primarily due to the increase in the steric repulsion between grafts (Figure 7b, top panel) overriding the corresponding increase in depletion attraction. The corresponding changes in the remaining two components—graft-to-core and core-to-graft repulsion—are smaller and in opposite directions and effectively cancel each other out. However, this is not the case for repulsion along $\mathbf{x}_{90^\circ}$, where the increase in graft-to-core repulsion is larger in magnitude than the decrease in the core-to-graft repulsion (middle panel). The residual repulsion from core−graft interactions, combined with

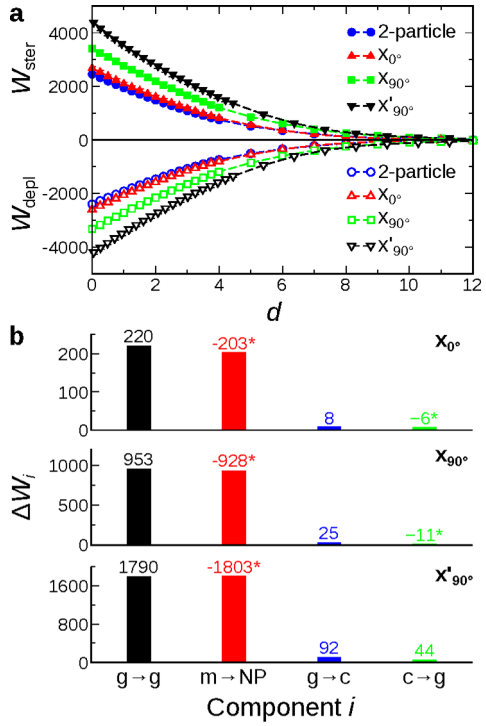

Figure 7. (a) Comparison of the net steric repulsion and depletion attraction experienced by the test NP along the two- and three-particle reaction coordinates. The two components nearly cancel each other, and the resulting PMF $W(d) = W_{ster}(d) + W_{depl}(d)$ for the different reaction coordinates are shown in Figure 3b. (b) Bar chart of the differences $\Delta W_i|_j \equiv W_i(0)|_{3\text{-particle},j} - W_i(0)|_{2\text{-particle}}$ in the values (specified above each bar) of the four PMF components $i \equiv$ g → g, m → NP, g → c, and c → g between the three- and two-particle configurations, calculated for each of the reaction coordinates $j \equiv \mathbf{x}_{0^\circ}$, $\mathbf{x}_{90^\circ}$, and $\mathbf{x}'_{90^\circ}$ at contact ($d = 0$). Negative values are marked with an asterisk and their bars are flipped towards positive side for easier comparison with positive values.

the stronger graft−graft repulsion versus depletion attraction, as in the case of $\mathbf{x}_{0^\circ}$, leads to even stronger repulsion along $\mathbf{x}_{90^\circ}$ as compared to $\mathbf{x}_{0^\circ}$ (Figure 3b). The situation is entirely different for the repulsion along $\mathbf{x}'_{90^\circ}$. Here, the increase in graft-to-graft repulsion is more than counterbalanced by the depletion attraction and the core-to-graft repulsion now increases instead of decreasing as in the case of $\mathbf{x}_{0^\circ}$ and $\mathbf{x}_{90^\circ}$ (bottom panel). Moreover, the core-to-graft and graft-to-core repulsion are both fairly strong and become the primary contributors to the very strong repulsion observed along $\mathbf{x}'_{90^\circ}$.

Effects of Polymer Grafts and Surrounding Matrix. To gain further insight into the influence of polymer grafting on the anisotropic interactions between the NPs, we extended our study to additional NP−polymer systems differing in the grafting density and/or graft length. Specifically, we examined nine different systems (Table 1, systems 1−9), resulting from combining three different grafting densities (Γ_g = 0.1, 0.2, and 0.4) and three different graft lengths (L_g = 5, 10, and 20), that includes the representative system with Γ_g = 0.4 and L_g = 20 discussed so far. Figure 8 compares the polymer-mediated repulsion $W_p(d)$ computed for these systems along $\mathbf{x}_{0^\circ}$, $\mathbf{x}_{90^\circ}$, and $\mathbf{x}'_{90^\circ}$. We find that the repulsion is very strong and differs significantly between the three reaction coordinates for large values of Γ_g and L_g. As these grafting parameters become smaller, the repulsion weakens and the $W_p(d)$ profiles for the three reaction coordinates become increasingly similar to each

DOI: 10.1021/acs.macromol.6b01936
Macromolecules XXXX, XXX, XXX−XXX

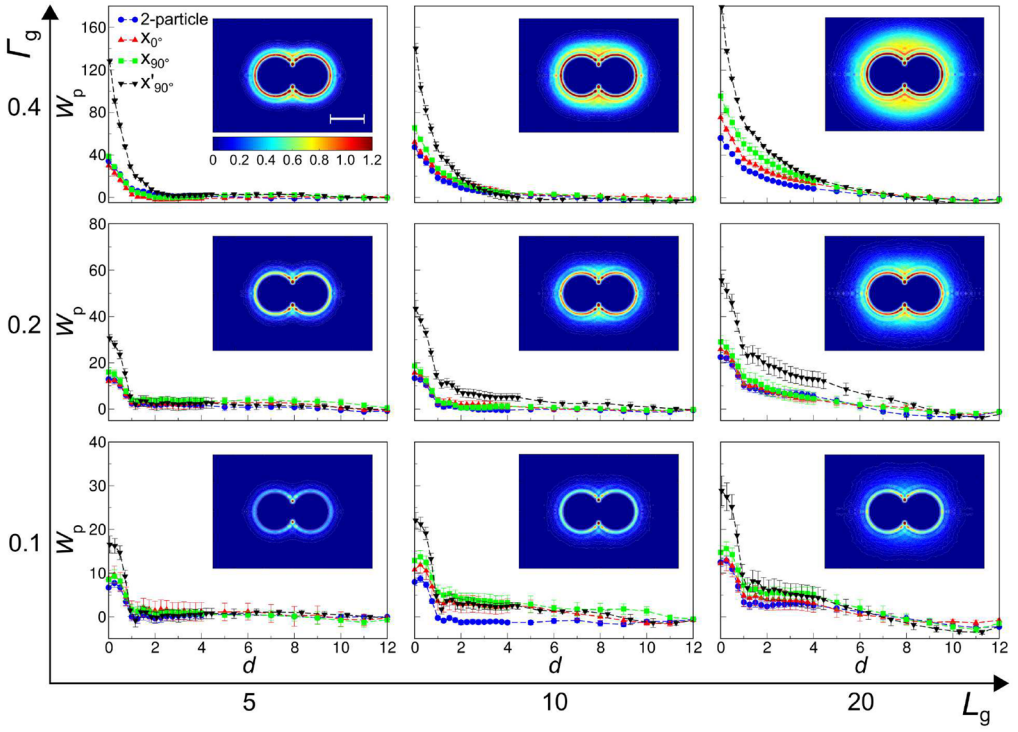

Figure 8. Polymer-mediated component of the PMF computed along the two- and three-particle reaction coordinates for nine distinct NP−polymer systems differing in NP graft length (L_g = 5, 10, 20) or grafting density (Γ_g = 0.1, 0.2, 0.4). Insets show the corresponding 2D contour maps of graft segmental density surrounding an isolated dimer (scale bar = 6σ).

other. In other words, the polymer-mediated repulsion is strongly anisotropic for long grafts and high grafting densities and becomes more isotropic as the grafts become shorter and more sparsely grafted. To further characterize this anisotropy as a function of graft length and grafting density, we computed the three-body contributions $\Delta W_3(d)$ for four of these NP−polymer systems differing in graft length and grafting density. Our results plotted in Figure 9 indicate that the interactions become increasingly anisotropic with increasing graft length and grafting density. In fact, for the lowest grafting density studied here (Γ_g = 0.1), the three-body contributions are negligible, even for relatively long grafts (Figures 9c,d).

The observed reduction in anisotropy with decreasing graft length and grafting density is easily explained from the graft

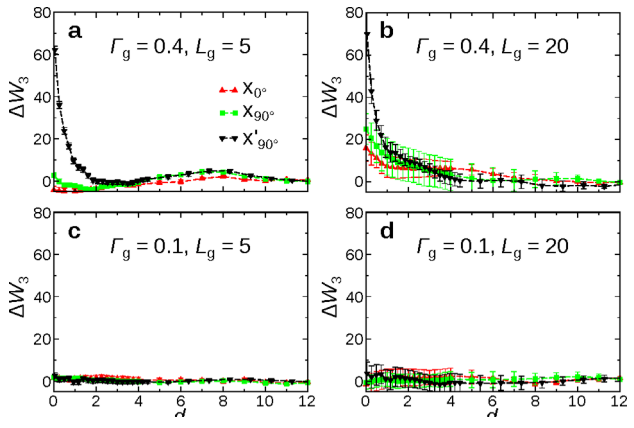

Figure 9. Three-body contribution $\Delta W_3(d)$ for four different NP−polymer systems differing in graft length and grafting density as specified in the figures along $\mathbf{x}_{0°}$, $\mathbf{x}_{90°}$, and $\mathbf{x}'_{90°}$.

segmental density maps $\rho_g(x,r)$ (Figure 8 insets): When either of the two grafting parameters is reduced, the high-density region depicted by the yellow−cyan halo around the NP cores changes from an anisotropic elliptical shape to a more isotropic shape that closely "hugs" the dimer surface. The strong correlation between the density contours and the PMFs reemphasizes the strong connection between anisotropy and graft segmental density. As expected, the overall segmental density (Figure S3) remains almost identical across all systems, again confirming the little-to-no correlation between anisotropy and overall segmental density. Dissecting $W_p(d)$ into steric and depletion contributions (Figure S4) reveals that both components are substantial for systems with high grafting density and long grafts and that the dominance of steric repulsion over depletion attraction results in strong polymer-mediated repulsion and large differences in the repulsion over the three reaction coordinates. As the grafting density and/or graft lengths become smaller, both components become weaker, leading to weaker overall repulsion and smaller differences in repulsion between the different reaction coordinates.

Our calculations have shown that the matrix chains produce strong depletion attraction between the NPs that negates much of the steric repulsion between them (Figure 7a). To further investigate the impact of the surrounding medium on the polymer-mediated repulsion between NPs, we examined the effects of replacing the matrix chains, currently of length L_m = 40, with shorter chains of length L_m = 20, 5, and 1, the last of which represents a "monomeric" solvent (Table 1, systems 10−12) ; We also examined the effect of removing the matrix altogether by considering NP interactions in vacuum (system 13). Figure 10 presents the $W_p(d)$ profiles computed for these new systems along $\mathbf{x}_{0°}$, $\mathbf{x}_{90°}$, and $\mathbf{x}'_{90°}$. Comparing against the

DOI: 10.1021/acs.macromol.6b01936
Macromolecules XXXX, XXX, XXX−XXX

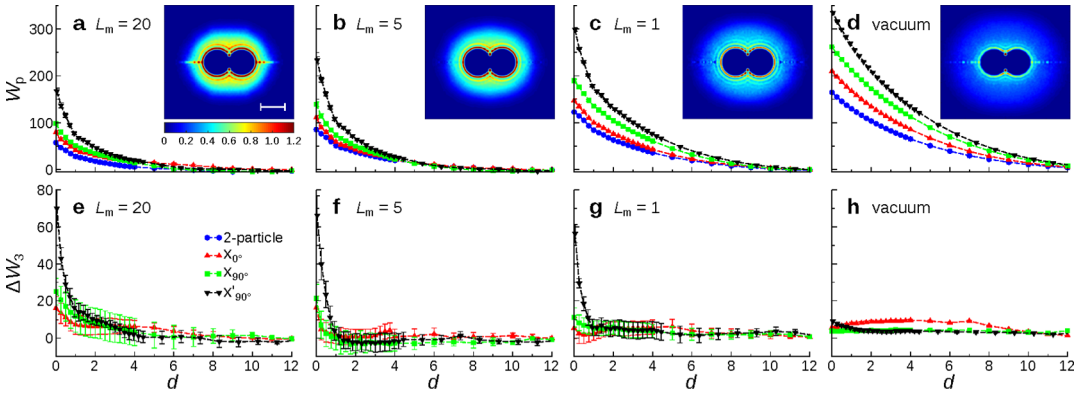

Figure 10. Polymer-mediated component of the PMF computed along the two- and three-particle reaction coordinates for NPs interacting across a polymer matrix of chain length (a) L_m = 20, (b) L_m = 5, (c) L_m = 1, and (d) L_m = 0 (vacuum), and their corresponding three-body contributions (e–h). Insets show the corresponding 2D contour maps of graft segmental density surrounding an isolated dimer (scale bar = 6σ).

profiles obtained for the reference system (Figure 3b), we find that decreasing the matrix chain length to L_m = 20 (Figure 10a) has no measurable effect on $W_p(d)$, and a further decrease to L_m = 5 leads to some (~40%) increase in repulsion (Figure 10b). However, dissolving the bonds between the matrix chain segments (L_m = 1) leads to a significant increase in repulsion, roughly twice in magnitude along each reaction coordinate (Figure 10c). The removal of matrix chains altogether leads to further increase in the strength of repulsion (Figure 10d). We note that each increase in the strength of repulsion with chain shortening is also accompanied by an outward extension in the range of repulsion. Also plotted in Figure 10 are the three-body contributions to the PMF, which are observed to decrease with the decreasing matrix chain length (Figure 10e–g) and, somewhat interestingly, become quite small when the matrix chains are removed altogether (Figure 10h). Thus, the presence of a matrix surrounding the polymer-grafted NPs seems to play an important role in enhancing three-body interactions between them.

To investigate the origin of this increase in the strength and range of repulsion with reduction in the length of the matrix chains and their subsequent removal, we turn to the graft segmental density maps (Figure 10 insets) and the steric and depletion components of $W_p(d)$ (Figure S5). The density maps clearly show that the NP grafts extend outward with the shortening and subsequent removal of matrix chains. This observation is consistent with the fact that the shorter the matrix chains, the weaker the depletion force (osmotic pressure) they exert (Figure S5) and thereby the farther the grafts extend into the matrix, which explains the observed increase in the range of repulsion with decreasing length and removal of matrix chains. Such extension of grafts also leads to a sparser layer of grafted polymer segments around the dimer NPs (Figure 10 insets), allowing easier interpenetration between the grafts of the test and dimer NPs. Thus, the diminishing depletion attraction with shortening and removal of matrix chains also results in smaller steric repulsion between grafts. However, this decrease in steric repulsion is smaller in magnitude than the corresponding decrease in depletion forces (Figure S5), which causes increase in the overall polymer-mediated repulsion with reduction in the length of the matrix chains or their removal. Though we did not study systems with matrix chains longer than 40 due to computational reasons, we expect their PMFs to look similar to those of L_m = 40 given that $W_p(d)$ and $\rho_g(x,r)$ seem to have converged at this chain length, indicating that the grafted chains are close to their maximum compression. The above results underscore the importance of the surrounding medium when examining interactions between NPs and suggest that the effects of the surrounding matrix cannot be neglected, even when the matrix is neutral to the grafts, as is the case in this study.

Additional Insights into Depletion Interactions. The polymer-grafted NPs examined here exhibit unusually strong depletion attraction, even in a monomeric matrix where the strength of the depletion interactions is ~1300 k_BT (Figure S5). To understand the origin of such strong interactions, we turn to the classical model of Asakura and Oosawa (AO model)[35,36] that provides an analytical expression for the strength of depletion interactions between two spherical particles in a solution of macromolecules (depletant). The model treats both components as hard spheres and uses an ideal-gas approximation to estimate the translational entropy that the macromolecules gain from the additional volume that frees up due to the overlap between the macromolecule-excluded volumes of two particles when they come into contact. Specifically, the free energy change ΔG_d resulting from the contact of two particles of diameter D_p in a surrounding solution of volume V containing N macromolecules of diameter D_m is given by[36]

$$\Delta G_d = -\frac{N\pi k_B T D_m{}^2(3D_p + 2D_m)}{12V} \quad (7)$$

where it was further assumed that V is much greater than the excluded volume overlap between the particles, applicable to most situations where the particles are present at low volume fraction.

We first investigated if the AO model could explain the large depletion attraction exhibited by our polymer-grafted NPs in a *monomeric* matrix. However, a straightforward application was not possible because eq 7 was derived for hard particles with an excluded volume defined by a sphere of diameter (D_p + D_m), while our NPs have a soft shell of polymer grafts around a hard core. If one considers the average height of the polymer grafts to be h_g and the diameter of the NP core to be D_c, the true excluded volume of the NP can be approximated as a sphere of diameter (D_c + $2h_g$ + 1), where 1 is the diameter of the depletant (monomeric segments) in reduced units. Thus, the diameter of the depletants D_m in eq 7 needs to be replaced by an "effective" diameter given by ($2h_g$ + 1). By substituing $h_g \approx$ 3.0 computed from simulations, $D_p = D_c$ = 6, and $N/V \equiv \rho_p$ =

DOI: 10.1021/acs.macromol.6b01936
Macromolecules XXXX, XXX, XXX–XXX

0.82, we obtained $\Delta G_d \approx -340\ k_BT$, which is of similar scale as the depletion attraction $W_{m\to NP}(0)$ computed from simulations. As reference, the AO depletion interactions for bare NPs of the same size in the same medium yielded only $\Delta G_d \approx -4\ k_BT$. Thus, the depletion interactions in polymer-grafted NPs can indeed be very large, primarily because they can exhibit an unusually large excluded volume overlap with other NPs due to their soft polymer grafts.

Next, we applied the model to polymer-grafted NPs in a *polymeric* matrix of length $L_m = 40$, where an entire matrix chain (depletant) was approximated as a hard sphere of diameter equal to $2R_g$, where R_g is the radius of gyration of the matrix chains; the effective diameter of the depletant now becomes equal to $(2h_g + 2R_g)$, and the depletant density N/V is given by ρ_p/L_m. By computing $R_g \approx 3.0$ from simulations, we obtained a value of $\Delta G \approx -25\ k_BT$, which is almost 2 orders of magnitude smaller than the value of $\sim 2500\ k_BT$ computed from simulations. Thus, the AO model does a poor job of estimating depletion interactions in polymer melts, as it neglects the gain in the internal configurational entropy of the chains, which can be substantial in melts. Nevertheless, to test the reasonableness of this huge depletion attraction observed in our simulations, we simulated the same system *but* containing bare NPs of diameters equal to the effective diameter $(D_c + 2h_g)$ of the polymer-grafted NPs and found that the depletion attraction is indeed comparable to that computed for polymer-grafted NPs (Figure S6).

It was noted earlier that the strength of the depletion attraction always goes hand-in-hand with that of steric repulsion and that the former is consistently weaker than the latter in all the systems investigated here, including two-particle configurations (see, for example, Figure 7a). The first observation is easily explained by recognizing that both types of forces increase with the amount of overlap between the grafts, and therefore if the steric repulsion were large due to a large overlap between grafts, the depletion attraction will also be large, and *vice versa*.

To explain the second observation, we consider the simpler case of a two-particle system composed of the test and reference NP (Figure 1c). In this system, the depletion force on the test NP arises due to differences in the population of matrix chains interacting with the inside and outside halves of the test NP (facing toward and away from the reference NP); Similarly, most of the steric force (>95% in Figure 6) on the test NP arises from its interactions with the grafts of the reference NP, which are clearly more populated on the inside half of the test NP. The observed dominance of steric forces over depletion forces could then be perceived to arise from the mismatch in population of reference NP grafts over the two halves of the test NP being larger than the corresponding mismatch in population of matrix chains.[37] To test this conjecture, we computed the differences $\Delta\rho_g$ and $\Delta\rho_m$ in the average density of polymer segments belonging to reference NP grafts and matrix chains within cylindrical volumes of radius R and thickness d touching the right and left poles of the test NP:

$$\Delta\rho_i = \frac{\int_0^R 2\pi r\ \mathrm{d}r \int_0^d [\rho_i(x, r) - \rho_i(D_c + 2d - x, r)]\ \mathrm{d}x}{\pi R^2 d} \tag{8}$$

where d is the surface-to-surface distance between the reference and test NP whose centers are assumed to be located at positions $x = -D_c/2$ and $x = D_c/2 + d$, and index i = g, m refers to the reference NP grafts or the matrix chains. We obtained $\Delta\rho_g = 0.33$, 0.31, and 0.25 and $\Delta\rho_m = -0.22$, -0.23, and -0.20 for the representative system (system 1, Table 1) at increasing separation $d = 2$, 4, and 6; for these calculations we employed $R = 6$, roughly corresponding to the footprint of a polymer-grafted NP (Figure 5). The positive $\Delta\rho_g$ indicates depletion of reference NP grafts on the outside region of the test NP, and the negative $\Delta\rho_m$ indicates depletion of matrix chains in the region between the reference and test NP. The decreasing magnitudes of $\Delta\rho_g$ and $\Delta\rho_m$ with increasing d indicates that the matrix and graft segmental densities become more isotropic around the test NP. More importantly, we find that the overall density difference $(\Delta\rho_g + \Delta\rho_m)$ is positive, suggesting a greater imbalance in the segmental density of grafted chains compared to matrix chains, explaining the slightly larger steric forces compared to depletion forces in this system.

Stability of NP Clusters and Phase Diagram. Experiments have shown that polymer-grafted NPs exhibit a rich phase diagram in which they transition from a dispersed morphology at sufficiently high grafting density and graft length to 1D strings to 2D sheets to 3D close-packed structures with decreasing grafting density and graft length. While it is not possible to directly relate the computed two- and three-particle PMFs to the stability of several of these higher-order structures due to multibody effects, such PMFs can nevertheless provide valuable information on the stabilities of small two- and three-particle clusters (dimer and trimer) as a function of parameters like grafting density and graft length. These clusters may be conceived as precursors of the 1D, 2D, and 3D higher-order structures. Note that each of the three-particle reaction coordinates yields a distinct configuration of the trimer: *linear*, *L-shaped*, and *triangular* configuration from $\mathbf{x}_{0^\circ}$, $\mathbf{x}_{90^\circ}$, or $\mathbf{x}'_{90^\circ}$, respectively. The "phase" diagram we seek therefore comprises five distinct phases: dispersed, dimer, and the three types of trimers.

We constructed such a phase diagram by *first* calculating the free energy change associated with forming a dimer or a trimer from isolated NPs. The free energy $\Delta G_{dim}(d)$ of forming a dimer with a surface-to-surface separation distance d is simply given by the two-particle PMF computed earlier that we *now* denote by $W_2(d)$:

$$\Delta G_{dim}(d) = W_2(d) \tag{9}$$

The free energy $\Delta G_{tri}(d_1,d_2)$ of forming any one of the three trimer configurations can be calculated as the sum of the free energies of first forming a dimer, as a function of distance d_1 between the dimer NPs, and then forming a trimer, as a function of distance d_2 between the third NP attaching onto the dimer:

$$\Delta G_{tri}(d_1, d_2) = W_2(d_1) + W_3^{2D}(d_2; d_1) \tag{10}$$

Here, $W_2(d_1)$ is the two-particle PMF computed earlier and $W_3^{2D}(d_2;d_1)$ is a 2D three-particle PMF that depends on both d_1 and d_2; Note that $W_3^{2D}(d_2;d_1)$ is *different* from the 1D three-particle PMFs computed thus far, and now denoted by $W_3(d)$, which consider interactions of a third NP with a dimer fixed at the contact distance $d_1 = 0$, that is, $W_3(d) \equiv W_3^{2D}(d;0)$.

The *next* step involves determining the global minimum in the computed ΔG_{dim} and ΔG_{tri} profiles that provides the relative stability of a structure. If this minimum free energy value is positive or if the entire profile is always positive, then that structure is deemed unstable. The stability of a dimer can

DOI: 10.1021/acs.macromol.6b01936
Macromolecules XXXX, XXX, XXX−XXX

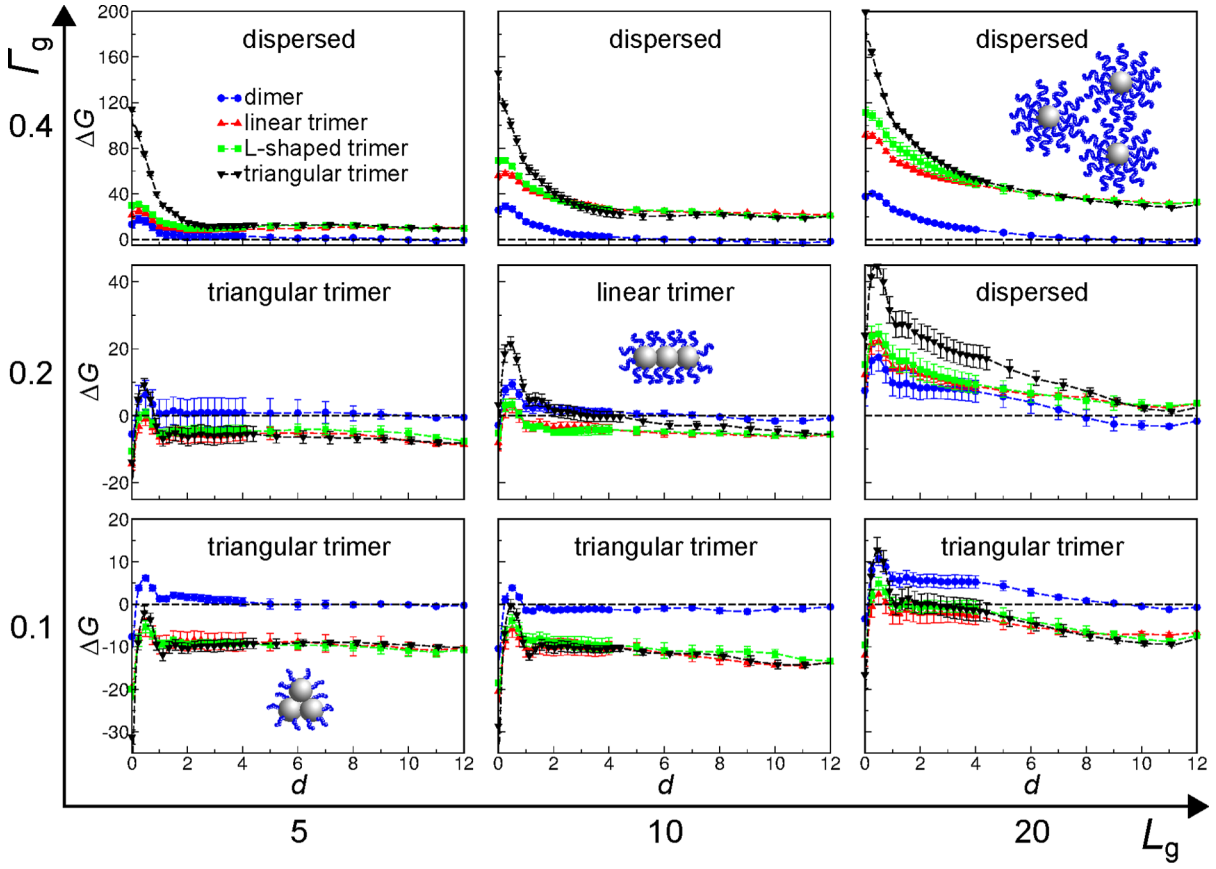

Figure 11. Free energies of formation of the NP-dimer $[\Delta G_{dim}(d)]$ and of the three different configurations of NP trimers $[\Delta G_{tri}(d)]$ for nine different kinds of polymer-grafted NPs in a polymer matrix of chain length $L_m = 40$. The NPs in all systems exhibit the same core−core attraction ($\epsilon_c = 1$), but differ in terms of their graft length ($L_g = 5, 10, 20$) or grafting density ($\Gamma_g = 0.1, 0.2, 0.4$).

be easily obtained as it involves computation of a 1D free energy profile, but determining the stability of the trimer phase is extremely computationally demanding, as it involves computation of a 2D three-particle PMF. To this end, we made the following reasonable approximation:

$$\min\{\Delta G_{tri}(d_1, d_2)\} \approx \min\{W_2(d_1)\} + \min\{W_3^{2D}(d_2; 0)\}$$
$$\equiv \min\{W_2(d)\} + \min\{W_3(d)\} \quad (11)$$

which allowed us to estimate the stability of the trimer clusters using only the already-computed PMFs. Note that we have assumed here that the minimum free energy of attaching the third NP is minimally affected by the precise configuration of the dimer as long as the dimer NPs are almost at touching distance in their most favorable configuration. This assumption is reasonable considering that (1) the most stable configuration of dimers are indeed ones in which the NPs are separated by small distances ($d_1 \approx 0.024\sigma$; see Figure 3a and earlier discussion) and (2) the PMF computed for system in which the dimer exhibits its most stable configuration ($d_1 \approx 0.024\sigma$) was found to be very similar to the three-particle PMF computed here with contacting dimer NPs ($d_1 = 0$) (see Figure S1 and earlier discussion). As explained earlier, the reason that our grafted NPs assemble at such close distances has to do with the short-ranged nature of vdW attraction between NPs as compared to polymer-mediated repulsion (compare Figures 3a and 3b). Therefore, we envision that for systems in which the vdW attraction is longer ranged, for instance when the size of the NPs is much larger and the attraction scales as $\sim 1/d$ or if the systems were so densely grafted that the NPs are unable to displace the grafts to access the strong vdW attraction.

Figure 11 compares the formation free energy profiles of the dimer and trimer phases for nine different combinations of graft lengths and grafting densities with the core−core attraction strength fixed at a value of $\epsilon_c = 1$ roughly corresponding to that of solid silicon. In particular, we compare $\Delta G_{dim}(d)$ and $\Delta G_{tri}(d)$, where the latter corresponds to the variation in the free energy of an NP trimer as a function of the distance between a NP and a NP-dimer already assembled and fixed in its most favorable configuration. We observe that the free energy profiles of the dimer and all three trimers are positive for $(L_g, \Gamma_g) = (20, 0.4)$, $(20, 0.2)$, $(10, 0.4)$, and $(5, 0.4)$. This implies that the NPs prefer to remain dispersed for such strongly grafted NPs, where the vdW attraction between the NP cores is too weak to overcome the polymer-mediated repulsion between the NPs. However, as the grafting density and graft length are reduced, the polymer-mediated repulsion becomes weaker, and the dimer and trimer phases begin to exhibit negative free energies of formation. In particular, we find that the linear trimer phase is the most stable phase at $(L_g, \Gamma_g) = (10, 0.2)$ while the triangular trimer phase becomes most stable at $(L_g, \Gamma_g) = (20, 0.1)$, $(10, 0.1)$, $(5, 0.2)$, and $(5, 0.1)$. In general, we find that the stability of the L-shaped trimer is always intermediate to that of the linear and triangular trimers and hence does not appear as the most stable phase under any grafting condition. We also note the presence of large energy barriers separating the associated and dispersed states. In cases where the bound state is globally stable, the presence of such

DOI: 10.1021/acs.macromol.6b01936
Macromolecules XXXX, XXX, XXX−XXX

energy barriers could cause the NPs to get kinetically trapped in the dispersed state, and thermal annealing of the polymer−NP system might be required to help NPs to cross over the barrier and bind to each other.

The above results on cluster stabilities along with those obtained for weaker (ϵ_c = 0.5) and stronger core/core attraction (ϵ_c = 3) are summarized in terms of phase diagrams in Figure 12. The general features of these phase diagrams

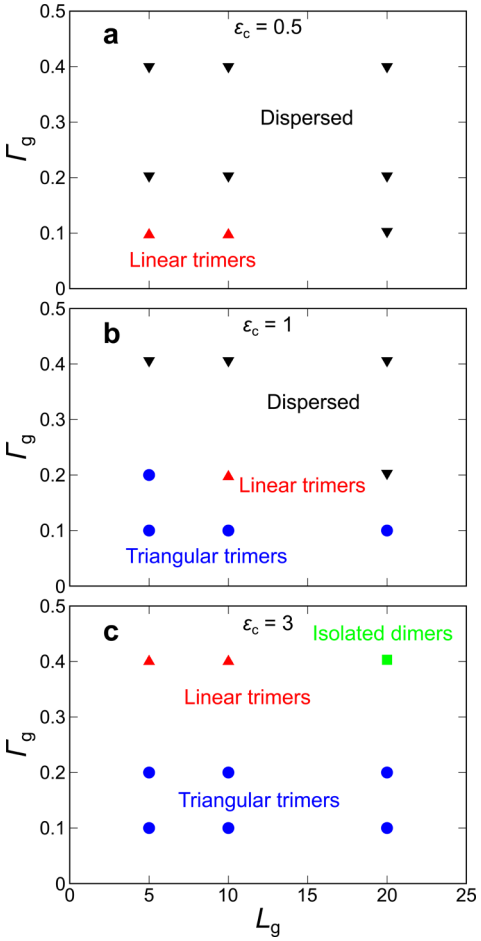

Figure 12. Phase diagrams along the graft length−grafting density parameter space depicting the most favorable configuration adopted by three NPs at different fixed values of the core−core attraction strength: (a) ϵ_c = 0.5, (b) ϵ_c = 1, and (c) ϵ_c = 3.

resemble those observed experimentally,[17] that is, the NPs transition from isotropic structures of high dimensionality (3D aggregates in experiments, triangular trimers here) to anisotropic structures of decreasing dimensionality (2D sheets to 1D strings in experiments, linear trimers to dimers here) with increasing grafting density and graft length, eventually yielding dispersed NPs (both here and in experiments) at sufficiently strong grafting conditions. As expected, a weak core−core attraction strength shifts the boundaries of the phases inward to small grafting densities and graft lengths, and *vice versa* for strong attraction.

Our phase diagrams also reveal a unique feature that is missing in the experimental phase diagram—the presence of a *globally* stable dimer phase (see Figure 12c). This phase appears within a small window of parameter space—arguably at high grafting densities, long grafts, and strong core/core attraction according to our results—where the two-particle PMF W_2 exhibits an attractive minimum while the three-particle PMF W_3 is purely repulsive due to the polymer redistribution effect discussed earlier. Within this region of the parameter space, the dimers are stable against dissociation into individual NPs and also stable against growing into trimers.

Since a linear trimer is less stable than the dimer in this region of the phase diagram, then we expect all *n*-particle *linear* structures (1D strings) to be less stable than the dimer, as each *j*-particle PMF $W_j(j > 3)$ is at least as repulsive as W_3. Now, it may be argued that the free energies of formation of other more compact higher-dimensional structures (such as tetragonally arranged tetramers, octahedrally arranged hexamers, etc.) may become lower than the formation free energy of the dimer. However, for that to occur, the *j*-particle PMF associated with the addition of an NP to a $(j-1)$-particle cluster would have to become strongly attractive, e.g., due to sudden jump in the vdW attraction W_c from an increase in the number of NP contacts, and more than counterbalance the strong polymer-mediated repulsion W_p arising from each of these contacting NPs, which is highly unlikely given that W_p increases stronger than linearly with the number of contacts (due to positive many-body contributions). Understandably, such compact higher-order structures appear only under weak grafting conditions (when the graft density/graft length are sufficiently small) in the experimental phase diagram, which is clearly incompatible with the strong grafting conditions under which the dimer phase is stabilized. Thus, we believe that the dimer phase identified here is also stable against forming higher-order structures. It would be interesting to experimentally test the existence of such a phase and to further investigate and map out its precise location within the grafting parameter space. Such stable NP-dimers, as well as other small clusters, could find applications in plasmonics.[10,38]

Note that one cannot make a similar claim about the global stability of any of the trimer configurations observed to be the most stable phase in our phase diagram. The reason is that though this phase has been determined to be averse to dissociating into lower-order structures (individual NPs, or dimer + isolated NP), it remains undetermined whether the phase is also averse to growing into larger structures (e.g., tetramers). In fact, when the trimer phase is determined to be stable, the three-particle PMF W_3 must be favorable (possess a minimum with negative free energy) according to eq 11. This would then imply that the four-particle PMF W_4 associated with attaching a fourth NP to the trimer would also likely be favorable, especially when the location of attachment is sufficiently far from other noncontacting NPs of the trimer in which case W_4 would be almost as favorable as W_3. The trimer would thus merely represent an intermediate to a more stable tetramer structure and so forth. Applying such an argument to a linear trimer would suggest that the trimer will continue to grow into a longer linear NP string as each NP addition to the ends of the string serves to further stabilize it. Similarly, the L-shaped and triangular trimer phases may be precursors of the square and hexagonal sheets, though we do not expect each subsequent addition of NP to yield the same free energy change as the three-particle PMF.

Lastly, we comment that the free energies of formation of clusters calculated from the PMFs ignore the loss in translational entropy and the gain in rotational entropy that NPs undergo upon assembly. The change in entropy associated

DOI: 10.1021/acs.macromol.6b01936
Macromolecules XXXX, XXX, XXX−XXX

with the dimerization of two NPs may be roughly estimated via[39]

$$\Delta S \approx k_B \left[\ln\left(\rho_N \left(\frac{h^2}{\pi m k_B T} \right)^{3/2} \right) + \ln\left(\frac{8\pi^2 I k_B T}{h^2} \right) - \frac{1}{2} \right] \tag{12}$$

where ρ_N is the number density of NPs, h is Planck's constant, m is the mass of each NP, and $I = mD_c^2/2$ is the moment of inertia of the NP-dimer. Using typical sizes (5−100 nm), densities (2−5 g/cm^3), and loadings (2−5 vol %) of NPs, we obtain ΔS in the range −9 to −18 k_B. Thus, the entropy change is small compared to the losses and gains in configurational entropy of the grafts and matrix chains (1000s of k_B according to Figure 6 and Figure S2). Hence, we expect the qualitative features of the phase diagram to be largely preserved even in the absence of this free energy component. Moreover, the translational entropy loss is expected to depend on the concentration of NPs. Therefore, the "standard" free energies of formation computed here do not depend on NP concentration, which facilitates easier comparison of the relative free energies of the structures as it does not require any specification of NP concentration.

CONCLUSIONS

We have investigated the role of polymer-mediated interactions between NPs in the formation of anisotropic structures from spherically symmetric polymer-grafted NPs by computing the overall PMF between a NP-dimer and a test NP along with its three-body contribution as a function of its orientation relative to the dimer. The rationale is that stable anisotropic phases like 1D strings and 2D sheets must emerge from an anisotropy in the three-body polymer-mediated component of the PMF because if that is not the case, the NPs would simply assemble into hexagonal close-packed aggregates to maximize the number of attractive contacts between the NPs or else remain dispersed if the attraction is weak. Our calculations show that the three-body, polymer-mediated component of the PMF is indeed highly anisotropic, exhibiting the strongest repulsion along the perpendicular axis passing through the center of the dimer and the least repulsion along its longitudinal axis. Further analysis reveals that this anisotropy, and the even stronger anisotropy observed in the overall PMFs, is directly related to the anisotropic distribution of graft segments near the surface of the dimer. In particular, the polymer grafts in between the dimer NPs get pushed outward from their contact point causing strong enhancement in the graft segmental density in the contact region in between the two NPs. The enhancement is highest within this region and gradually decreases away from it, reaching its lowest value at the dimer poles, similar to the observed variation in polymer-mediated repulsion. By decomposing the polymer-mediated PMF into steric repulsion arising from the grafted chains and depletion interactions arising from the surrounding matrix, we find that the reduction in the grafted polymer density from dimer contact region to its poles leads to concomitant reduction in steric and depletion interactions along the same direction. However, with the steric repulsion consistently dominating depletion attraction, the net effect is a reduction in polymer-mediated repulsion from the contact region to the poles. This consistent dominance of steric over depletion forces seems to arise from a greater mismatch in the segmental density of grafted chains, as opposed to that of matrix chains, across the inner and outer halves of the interacting NPs. Interestingly, despite the strong variation in the graft segmental density, the overall segmental density remains independent of location around the dimer surface.

Probing further the role of the NP grafts and the surrounding matrix, the anisotropy in both the overall and three-body contribution of polymer-mediated interactions is found to intensify with increasing graft length and grafting density. This trend arises again due to the simultaneous rise in the steric repulsion and depletion attraction, and the increasing dominance of the former over the latter, with increasing graft length and grafting density. The surrounding matrix has a very different effect, where the anisotropy in the overall PMF is found to diminish with increasing length of matrix chains. In fact, NPs interacting in a monomeric matrix at the same density as the polymer matrix exhibit much higher anisotropy, and those interacting in a vacuum exhibit even higher anisotropy. The strength of and anisotropy in the three-body component, in contrast, is found to increase with increasing matrix chain length. Our analysis shows that even though both depletion and steric forces decrease rapidly with the monomerization and subsequent removal of matrix chains, the steric forces decrease less rapidly than the depletion forces, leading to increasing anisotropy in polymer-mediated repulsion. Additional analysis reveals that the unusually large depletion forces observed in polymer-grafted NPs arises from the ability of their grafts to overlap when they come into close contact, leading to unusually large changes in the matrix-excluded volume.

Representative overall PMFs, obtained by adding an attractive vdW core/core potential to the polymer-mediated PMF, lead to complex behavior. While vdW attraction favors the formation of triangular three-particle clusters and polymer-mediated repulsion favors (least disfavors) linear clusters, the overall PMF stipulates that all three cluster configurations (triangular, L-shaped, or linear) may be stable depending on the relative strengths of the two PMF components. The overall PMFs also provide some basis for the experimentally observed anisotropic phases given that the triangular, L-shaped, and linear three-particle clusters may be conceived as precursors of the 2D hexagonal, 2D square, and 1D string phases and that the three cluster configurations were found to occupy *qualitatively* similar regions of the parameter space as the three higher-order anisotropic phases. Lastly, our cluster phase diagram predicts the possibility of observing a stable NP-dimer phase within a narrow window of parameter space where the two-particle PMF is attractive and all three-particle PMFs are repulsive. The existence of this novel phase with potential applications in plasmonics remains to be tested.

ASSOCIATED CONTENT

Supporting Information

The Supporting Information is available free of charge on the ACS Publications website at DOI: 10.1021/acs.macromol.6b01936.

Three-particle polymer-mediated repulsion with relaxed dimer configuration, entropic and energetic contributions of graft−graft repulsion; overall segmental density maps as a function of graft length and grafting density; comparison of steric repulsion and depletion attraction as a function of graft length, grafting density, and matrix chain length; and comparison of depletion attraction between grafted- and bare-NPs (PDF)

DOI: 10.1021/acs.macromol.6b01936
Macromolecules XXXX, XXX, XXX−XXX

AUTHOR INFORMATION

Corresponding Author

*E-mail garya@ucsd.edu; Ph 858-822-5542; Fax 858-534-9553 (G.A.).

ORCID

Gaurav Arya: 0000-0002-5615-0521

Notes

The authors declare no competing financial interest.

ACKNOWLEDGMENTS

We thank the National Science Foundation (CMMI, Grant No. 1200850) and the American Chemical Society Petroleum Research Fund (Award No. 52515-ND7) for partial support of this research. Computational resources were provided by the Extreme Science and Engineering Discovery Environment (XSEDE) Program, which is supported by the National Science Foundation Grant ACI-1053575. T.-Y.T. is supported by a scholarship from the Yin Chin Foundation of U.S.A and STUF United Fund Inc.

REFERENCES

(1) Grzelczak, M.; Vermant, J.; Furst, E. M.; Liz-Marzán, L. M. Directed self-assembly of nanoparticles. *ACS Nano* **2010**, *4*, 3591−3605.

(2) Nie, Z.; Petukhova, A.; Kumacheva, E. Properties and emerging applications of self-assembled structures made from inorganic nanoparticles. *Nat. Nanotechnol.* **2010**, *5*, 15−25.

(3) Glotzer, S. C.; Solomon, M. J. Anisotropy of building blocks and their assembly into complex structures. *Nat. Mater.* **2007**, *6*, 557−562.

(4) Peng, X.; Manna, L.; Yang, W.; Wickham, J.; Scher, E.; Kadavanich, A.; Alivisatos, A. P. Shape control of CdSe nanocrystals. *Nature* **2000**, *404*, 59−61.

(5) Tao, A. R.; Habas, S.; Yang, P. Shape control of colloidal metal nanocrystals. *Small* **2008**, *4*, 310−325.

(6) Miszta, K.; de Graaf, J.; Bertoni, G.; Dorfs, D.; Brescia, R.; Marras, S.; Ceseracciu, L.; Cingolani, R.; van Roij, R.; Dijkstra, M. Hierarchical self-assembly of suspended branched colloidal nanocrystals into superlattice structures. *Nat. Mater.* **2011**, *10*, 872−876.

(7) Manna, L.; Scher, E. C.; Alivisatos, A. P. Synthesis of soluble and processable rod-, arrow-, teardrop-, and tetrapod-shaped CdSe nanocrystals. *J. Am. Chem. Soc.* **2000**, *122*, 12700−12706.

(8) Henzie, J.; Grünwald, M.; Widmer-Cooper, A.; Geissler, P. L.; Yang, P. Self-assembly of uniform polyhedral silver nanocrystals into densest packings and exotic superlattices. *Nat. Mater.* **2011**, *11*, 131−137.

(9) Zanella, M.; Bertoni, G.; Franchini, I. R.; Brescia, R.; Baranov, D.; Manna, L. Assembly of shape-controlled nanocrystals by depletion attraction. *Chem. Commun.* **2011**, *47*, 203−205.

(10) Gao, B.; Arya, G.; Tao, A. R. Self-orienting nanocubes for the assembly of plasmonic nanojunctions. *Nat. Nanotechnol.* **2012**, *7*, 433−437.

(11) Gröschel, A. H.; Walther, A.; Löbling, T. I.; Schacher, F. H.; Schmalz, H.; Müller, A. H. Guided hierarchical co-assembly of soft patchy nanoparticles. *Nature* **2013**, *503*, 247−251.

(12) Du, J.; O'Reilly, R. K. Anisotropic particles with patchy, multicompartment and Janus architectures: preparation and application. *Chem. Soc. Rev.* **2011**, *40*, 2402−2416.

(13) O' Brien, M. N.; Jones, M. R.; Lee, B.; Mirkin, C. A. Anisotropic nanoparticle complementarity in DNA-mediated co-crystallization. *Nat. Mater.* **2015**, *14*, 833−839.

(14) Lattuada, M.; Hatton, T. A. Preparation and controlled self-assembly of Janus magnetic nanoparticles. *J. Am. Chem. Soc.* **2007**, *129*, 12878−12889.

(15) Sear, P.; Chung, S. W.; Markovich, G.; Gelbart, W. M.; Heath, J. R. Spontaneous patterning of quantum dots at the air-water interface. *Phys. Rev. E: Stat. Phys., Plasmas, Fluids, Relat. Interdiscip. Top.* **1999**, *59*, R6255−R6258.

(16) Malescio, G.; Pellicane, G. Stripe phases from isotropic repulsive interactions. *Nat. Mater.* **2003**, *2*, 97−100.

(17) Akcora, P.; Liu, H.; Kumar, S. K.; Moll, J.; Li, Y.; Benicewicz, B. C.; Schadler, L. S.; Acehan, D.; Panagiotopoulos, A. Z.; Pryamitsyn, V.; Ganesan, V.; Ilavsky, J.; Thiyagarajan, P.; Colby, R. H.; Douglas, J. F. Anisotropic self-assembly of spherical polymer-grafted nanoparticles. *Nat. Mater.* **2009**, *8*, 354−359.

(18) Bedrov, D.; Smith, G. D.; Li, L. Molecular Dynamics Simulation Study of the Role of Evenly Spaced Poly(ethylene oxide) Tethers on the Aggregation of C60 Fullerenes in Water. *Langmuir* **2005**, *21*, 5251−5255.

(19) Srivastava, S.; Agarwal, P.; Archer, L. A. Tethered nanoparticle-polymer composites: phase stability and curvature. *Langmuir* **2012**, *28*, 6276−6281.

(20) Jiao, Y.; Akcora, P. Assembly of polymer-grafted magnetic nanoparticles in polymer melts. *Macromolecules* **2012**, *45*, 3463−3470.

(21) Koerner, H.; Drummy, L. F.; Benicewicz, B.; Li, Y.; Vaia, R. A. Nonisotropic self-organization of single-component hairy nanoparticle assemblies. *ACS Macro Lett.* **2013**, *2*, 670−676.

(22) Pryamtisyn, V.; Ganesan, V.; Panagiotopoulos, A. Z.; Liu, H.; Kumar, S. K. Modeling the anisotropic self-assembly of spherical polymer-grafted nanoparticles. *J. Chem. Phys.* **2009**, *131*, 221102.

(23) Hattemer, G. D.; Arya, G. Viscoelastic Properties of Polymer-Grafted Nanoparticle Composites from Molecular Dynamics Simulations. *Macromolecules* **2015**, *48*, 1240−1255.

(24) Kremer, K.; Grest, G. S. Dynamics of entangled linear polymer melts: A molecular-dynamics simulation. *J. Chem. Phys.* **1990**, *92*, 5057−5086.

(25) Weeks, J. D.; Chandler, D.; Andersen, H. C. Role of repulsive forces in determining the equilibrium structure of simple liquids. *J. Chem. Phys.* **1971**, *54*, 5237−5247.

(26) Rakhmanov, E. A.; Saff, E.; Zhou, Y. Minimal discrete energy on the sphere. *Math. Res. Lett.* **1994**, *1*, 647−662.

(27) Saff, E. B.; Kuijlaars, A. B. Distributing many points on a sphere. *mathematical intelligencer* **1997**, *19*, 5−11.

(28) Carter, E.; Ciccotti, G.; Hynes, J. T.; Kapral, R. Constrained reaction coordinate dynamics for the simulation of rare events. *Chem. Phys. Lett.* **1989**, *156*, 472−477.

(29) Sprik, M.; Ciccotti, G. Free energy from constrained molecular dynamics. *J. Chem. Phys.* **1998**, *109*, 7737−7744.

(30) Guardia, E.; Rey, R.; Padró, J. Potential of mean force by constrained molecular dynamics: a sodium chloride ion-pair in water. *Chem. Phys.* **1991**, *155*, 187−195.

(31) Arya, G. Chain stiffness and attachment-dependent attraction between polyelectrolyte-grafted colloids. *J. Phys. Chem. B* **2010**, *114*, 15886−15896.

(32) Nosé, S. Constant temperature molecular dynamics methods. *Prog. Theor. Phys. Suppl.* **1991**, *103*, 1−46.

(33) Plimpton, S. Fast parallel algorithms for short-range molecular dynamics. *J. Comput. Phys.* **1995**, *117*, 1−19.

(34) Grest, G. S. Communication: Polymer entanglement dynamics: Role of attractive interactions. *J. Chem. Phys.* **2016**, *145*, 141101.

(35) Asakura, S.; Oosawa, F. On interaction between two bodies immersed in a solution of macromolecules. *J. Chem. Phys.* **1954**, *22*, 1255−1256.

(36) Asakura, S.; Oosawa, F. Interaction between particles suspended in solutions of macromolecules. *J. Polym. Sci.* **1958**, *33*, 183−192.

(37) Meng, D.; Kumar, S. K.; Lane, J. M. D.; Grest, G. S. Effective interactions between grafted nanoparticles in a polymer matrix. *Soft Matter* **2012**, *8*, 5002−5010.

(38) Fan, J. A.; Wu, C.; Bao, K.; Bao, J.; Bardhan, R.; Halas, N. J.; Manoharan, V. N.; Nordlander, P.; Shvets, G.; Capasso, F. Self-assembled plasmonic nanoparticle clusters. *Science* **2010**, *328*, 1135−1138.

(39) Steinberg, I. Z.; Scheraga, H. A. Entropy changes accompanying association reactions of proteins. *J. Biol. Chem.* **1963**, *238*, 172−181.

DOI: 10.1021/acs.macromol.6b01936
Macromolecules XXXX, XXX, XXX−XXX